Monthly Notices
of the
ROYAL ASTRONOMICAL SOCIETY

MNRAS **483,** 2078–2099 (2019)
Advance Access publication 2018 November 21

doi:10.1093/mnras/sty3143

Cosmological information in the redshift-space bispectrum

Victoria Yankelevich★ and Cristiano Porciani★†

Argelander-Institut für Astronomie, University of Bonn, Auf dem Hügel 71, D-53121 Bonn, Germany

Accepted 2018 November 16. Received 2018 November 16; in original form 2018 July 18

ABSTRACT

We use the Fisher-matrix formalism to investigate whether the galaxy bispectrum in redshift space, B, contains additional cosmological information with respect to the power spectrum, P. We focus on a *Euclid*-like survey and consider cosmological models dominated by dark energy and cold dark matter with Gaussian primordial perturbations. After discussing the phenomenology of redshift-space distortions for the bispectrum, we derive an expression for the cross-covariance between B and P at leading order in perturbation theory. Our equation generalizes previous results that did not consider binning in the orientation of wavevector triangles with respect to the line of sight. By considering Fourier modes with wavenumber $k < 0.15\,h\,\mathrm{Mpc}^{-1}$, we find that B and P set similar constraints on the cosmological parameters. Generally, error bars moderately improve when the two probes are combined together. For instance, the joint 68.3 per cent credible region for the parameters that describe a dynamical dark-energy equation of state shrinks by a factor of 2.6 with respect to only using the power spectrum. Regrettably, this improvement is cancelled out when the clustering analysis is combined with priors based on current studies of the cosmic microwave background. In this case, combining B and P does not give any appreciable benefit other than allowing a precise determination of galaxy bias. Finally, we discuss how results depend on the binning strategy for the clustering statistics as well as on the maximum wavenumber. We also show that only considering the bispectrum monopole leads to a significant loss of information.

Key words: cosmology: cosmological parameters – cosmology: dark energy – cosmology: large-scale structure of Universe.

1 INTRODUCTION

The last decades have witnessed a tremendous increase in the size of galaxy redshift catalogues that culminated in the completion of the Two-degree Field Galaxy Redshift Survey (2dFGRS) and the Sloan Digital Sky Survey (SDSS) as well as their more recent extensions. The scientific output of these efforts have been unprecedented and contributed to fostering several fields of astrophysics. The detection of baryonic acoustic oscillations in the galaxy two-point statistics (Cole et al. 2005; Eisenstein et al. 2005) was a major breakthrough in cosmology, as it allowed us to measure the distance–redshift relation on large scales and thus reconstruct the expansion history of the Universe.

Still, there is need for conducting even wider and deeper observational campaigns to address several key issues: (i) the nature of dark energy and dark matter, (ii) the neutrino masses, (iii) the statistical properties of primordial density fluctuations. These are the main science drivers of the planned next generation of surveys that will be conducted, for instance, with the Dark Energy Spectroscopic Instrument (DESI; DESI Collaboration et al. 2016a,b), the *Euclid* satellite (Laureijs et al. 2011), and the Square Kilometre Array (SKA; Maartens et al. 2015).

It is customary to extract cosmological information from galaxy catalogues using the two-point correlation function or its Fourier transform, the power spectrum. Either of these functions fully characterize a zero-mean Gaussian random field. However, the galaxy distribution displays complex patterns characterized by elongated filaments, compact clusters, and volume-filling underdense regions. These features are not captured by two-point statistics that do not retain information on the phases of the Fourier modes of the galaxy distribution. Therefore, if measured with sufficient accuracy and precision, higher-order statistics like the n-point correlation functions (with $n > 2$) and their Fourier transforms, the polyspectra, should contain additional information.

Until recently, galaxy redshift surveys could only provide rather noisy and imprecise measurements of higher-order statistics (Jing & Börner 1998; Frieman & Gaztañaga 1999; Scoccimarro et al. 2001; Verde et al. 2002; Croton et al. 2004; Jing & Börner 2004; Kulkarni et al. 2007; Gaztañaga et al. 2009; Marín 2011). In fact, the presence or the absence of rare large-scale structures within the

★ E-mail: vyankelevich@astro.uni-bonn.de (VY); porciani@astro.uni-bonn.de (CP)

† Member of the International Max Planck Research School (IMPRS) for Astronomy and Astrophysics at the Universities of Bonn and Cologne.

surveyed volume can shift the estimated statistics significantly thus calling for the need to build statistically representative samples that cover larger volumes (Croton et al. 2004; Gaztañaga et al. 2005; Nichol et al. 2006). For this reason, there is a lack of dedicated tools (theoretical predictions, estimators, likelihood models) to analyse higher-order statistics with respect to those specifically developed for the power spectrum. However, the situation is gradually changing as surveys cover unprecedentedly large volumes sampled with high galaxy number densities (Gil-Marín et al. 2015, 2017; Slepian et al. 2017). In particular, the bispectrum will be robustly and accurately measured with the advent of the above-mentioned experiments of the next generation. Developing techniques for exploiting the galaxy bispectrum is thus necessary to maximize the scientific return of these missions.

Historically, the bispectrum has been considered as a useful tool to learn about the statistical properties of the primordial density perturbations that seeded structure formation (their degree of non-Gaussianity, in particular) and to study non-linear physical processes like gravitational dynamics and galaxy biasing. Since these processes generate different functional dependences on the triangular configurations, they can be disentangled by fitting the measurements with theoretical templates. This procedure, for instance, removes the degeneracy between the galaxy linear bias coefficient and the amplitude of the dark-matter perturbations invariably found in power-spectrum studies (e.g. Fry 1994; Matarrese, Verde & Heavens 1997; Sefusatti et al. 2006).

Forecasts for the constraining power of the galaxy bispectrum usually determine the expected uncertainty for the bias and/or non-Gaussianity coefficients by assuming the main cosmological parameters are known exactly (Scoccimarro, Sefusatti & Zaldarriaga 2004; Sefusatti & Komatsu 2007; Song, Taruya & Oka 2015; Tellarini et al. 2016; Yamauchi, Yokoyama & Takahashi 2017a; Karagiannis et al. 2018). This strategy has been recently extended to modified theories of gravity (Yamauchi, Yokoyama & Tashiro 2017b). In this paper, we follow a different approach and use the Fisher-matrix formalism to quantify the potential of the bispectrum as a means to extract additional cosmological information with respect to traditional power-spectrum studies. For surveys of the previous generation, a similar analysis has been presented by Sefusatti et al. (2006), who made forecasts for the combination of galaxy-clustering data from SDSS North with the analysis of the cosmic microwave background (CMB) performed by the *Wilkinson Microwave Anisotropy Probe* (*WMAP*). Given the substantially improved perspectives for studies of galaxy clustering, it is imperative to update the prior investigation by utilizing the characteristics of the forthcoming surveys. Recent related work focuses either on developing optimal compression algorithms for three-point statistics (Byun et al. 2017; Gualdi et al. 2018a) or on detecting primordial non-Gaussianity due to the presence of massive spinning particles during inflation (Moradinezhad Dizgah et al. 2018). Here, we discuss the advantages (or lack thereof) of combining measurements of the galaxy power spectrum and bispectrum to constrain the standard cosmological parameters and, in particular, the dark-energy equation of state. In order to provide a concrete example, we focus on a *Euclid*-like survey and consider flat cosmological models dominated by dark energy and cold dark matter (CDM) with Gaussian primordial perturbations. We also combine the constraints from the clustering data with those from the CMB analysis by the *Planck* mission. Apart from considering data sets of current interest, we improve upon Sefusatti et al. (2006) in multiple other ways. For instance, we (i) consider the full galaxy bispectrum in redshift space instead of its monopole moment, (ii) make forecasts for dynamical dark-energy models, and (iii) account for a more sophisticated bias expansion that also depends on the tidal field and which represents the current state of the art. We are interested in the constraining power of two- and three-point statistics of the actual galaxy distribution in redshift space. Therefore, as a first step, we neglect observational limitations that will somewhat reshuffle and degrade the information. For example, we only approximately take into account the survey geometry through our binning strategy and neglect the Alcock–Paczynski effect (as in Sefusatti et al. 2006). These issues will be accounted for in our future work.

The paper is organized as follows. In Section 2, we introduce our notation and define the relevant statistical quantities. In Section 3, we briefly summarize the Fisher-matrix formalism and describe the set-up of our study. Our results are presented in Section 4 and discussed in Section 5. Finally, in Section 6, we conclude.

2 GALAXY STATISTICS

2.1 Power spectrum and bispectrum

Given a galaxy population, we model its spatial distribution at fixed time as the discrete sampling of a continuous random field $\rho_{\rm g}(\boldsymbol{x})$ which gives the local galaxy density per unit comoving volume in the expanding Universe. We assume that $\delta_{\rm g}(\boldsymbol{x})$ is statistically homogeneous, i.e. that all its connected n-point correlation functions are invariant under spatial translations. After defining the mean galaxy density $\bar{\rho}_{\rm g} = \langle \rho_{\rm g}(\boldsymbol{x}) \rangle$ (the brackets here denote averages taken over an ideal ensemble of realisations), we introduce the dimensionless overdensity as

$$\delta_{\rm g}(\boldsymbol{x}) = \frac{\rho_{\rm g}(\boldsymbol{x})}{\bar{\rho}_{\rm g}} - 1 \,. \tag{1}$$

We would like to decompose $\delta_{\rm g}(\boldsymbol{x})$ into simple oscillatory functions like plane waves. For a generic absolutely integrable function $f(\boldsymbol{x})$, we can write

$$f(\boldsymbol{x}) = \int \tilde{f}(\boldsymbol{k})\, {\rm e}^{i\boldsymbol{k}\cdot\boldsymbol{x}}\, \frac{{\rm d}^3k}{(2\pi)^3} \,, \tag{2}$$

where

$$\tilde{f}(\boldsymbol{k}) = \int f(\boldsymbol{x})\, {\rm e}^{-i\boldsymbol{k}\cdot\boldsymbol{x}}\, {\rm d}^3x \tag{3}$$

denotes the Fourier transform of $f(\boldsymbol{x})$. However, $\delta_{\rm g}(\boldsymbol{x})$ cannot be Fourier transformed as, in almost all realisations, the integral $\int |\delta_{\rm g}(\boldsymbol{x})|\, {\rm d}^3x$ diverges when taken over all space. Therefore, we consider a finite region of volume V and define a 'sample function' $\delta_V(\boldsymbol{x})$ such that $\delta_V(\boldsymbol{x}) = \delta_{\rm g}(\boldsymbol{x})$ if $\boldsymbol{x} \in V$ and $\delta_V(\boldsymbol{x}) = 0$ if $\boldsymbol{x} \notin V$. The power spectral density of $\delta_{\rm g}(\boldsymbol{x})$ can be defined as

$$P(\boldsymbol{k}) = \lim_{V\to\infty} \frac{\langle |\tilde{\delta}_V(\boldsymbol{k})|^2 \rangle}{V} = \lim_{V\to\infty} \frac{\langle \tilde{\delta}_V(\boldsymbol{k})\, \tilde{\delta}_V(-\boldsymbol{k}) \rangle}{V} , \tag{4}$$

where the limit exists only if it is performed after taking the ensemble average. In general, we can write

$$\langle \tilde{\delta}_V(\boldsymbol{k})\, \tilde{\delta}_V(\boldsymbol{q}) \rangle = \int \xi(r)\, {\rm e}^{-i\boldsymbol{k}\cdot\boldsymbol{r}}\, {\rm d}^3r \int_V {\rm e}^{-i(\boldsymbol{k}+\boldsymbol{q})\cdot\boldsymbol{x}}\, {\rm d}^3x , \tag{5}$$

where $\xi(\boldsymbol{r}) = \langle \delta_{\rm g}(\boldsymbol{x})\, \delta_{\rm g}(\boldsymbol{x}+\boldsymbol{r}) \rangle$ denotes the two-point correlation function of $\delta_{\rm g}(\boldsymbol{x})$ and the first integral runs over all separation vectors $\boldsymbol{r} = \boldsymbol{y} - \boldsymbol{x}$ such that $(\boldsymbol{x}, \boldsymbol{y}) \in V \times V$. Taking the limit for $V \to \infty$ and extending the definitions above to generalized functions, we obtain

$$\lim_{V\to\infty} \left\langle \tilde{\delta}_V(\boldsymbol{k})\, \tilde{\delta}_V(\boldsymbol{k}') \right\rangle = (2\pi)^3\, P(\boldsymbol{k})\, \delta_{\rm D}(\boldsymbol{k}+\boldsymbol{k}') \,, \tag{6}$$

where $\delta_{\rm D}(\boldsymbol{k})$ denotes the three dimensional Dirac delta distribution and the power spectrum $P(\boldsymbol{k})$ is the Fourier transform of $\xi(\boldsymbol{r})$.

Similarly, at the three-point level, we can write

$$B(\boldsymbol{k}_1,\boldsymbol{k}_2,\boldsymbol{k}_3)=\lim_{V\to\infty}\frac{\langle\tilde{\delta}_V(\boldsymbol{k}_1)\,\tilde{\delta}_V(\boldsymbol{k}_2)\,\tilde{\delta}_V(-\boldsymbol{k}_1-\boldsymbol{k}_2)\rangle}{V}\,, \tag{7}$$

or, equivalently,

$$\lim_{V\to\infty}\left\langle\tilde{\delta}_V(\boldsymbol{k}_1)\,\tilde{\delta}_V(\boldsymbol{k}_2)\,\tilde{\delta}_V(\boldsymbol{k}_3)\right\rangle= (2\pi)^3\,B(\boldsymbol{k}_1,\boldsymbol{k}_2,\boldsymbol{k}_3)\,\delta_{\rm D}(\boldsymbol{k}_{123})\,, \tag{8}$$

where $B(\boldsymbol{k}_1,\boldsymbol{k}_2,\boldsymbol{k}_3)$ defines the galaxy bispectrum (i.e. the Fourier transform of the connected three-point correlation function) and $\boldsymbol{k}_{123}=\boldsymbol{k}_1+\boldsymbol{k}_2+\boldsymbol{k}_3$, meaning that the bispectrum is defined only for closed triangles of wavevectors.

Different statistics (based on alternative expansions with respect to the Fourier decompositions) need to be employed to analyse samples that cover a wide solid angle on the sky (e.g. Fisher, Scharf & Lahav 1994; Heavens & Taylor 1995; Pápai & Szapudi 2008).

2.2 Redshift-space distortions

We infer the comoving position of a galaxy by using two observables (position on the sky and redshift) and by assuming that the photons we receive from it propagate in an unperturbed Friedmann–Robertson–Walker model universe. The resulting galaxy distribution in this 'redshift space' provides a distorted representation of the actual one in 'real space' due to the presence of inhomogeneities and peculiar velocities. The latter generate the largest distortions (Jackson 1972; Sargent & Turner 1977; Kaiser 1987; Hamilton 1998) that dominate over other relativistic effects (see e.g. Borzyszkowski, Bertacca & Porciani 2017, and references therein) that we will neglect in this work.

Although the galaxy distribution in real space is statistically isotropic (implying that $P(\boldsymbol{k})$ only depends on the magnitude k and $B(\boldsymbol{k}_1,\boldsymbol{k}_2,\boldsymbol{k}_3)$ on the three values k_1, k_2, and k_3), redshift-space distortions (RSD) break this isotropy and introduce some angular dependences. In the distant-observer approximation, when galaxy separations are much smaller than the distance from the observer to the galaxies so that a single line of sight $\hat{\boldsymbol{s}}$ can be defined for the whole sample, the power spectrum in redshift space depends on k and $\mu=(\boldsymbol{k}\cdot\hat{\boldsymbol{s}})/k$. This result derives from the fact that density and velocity perturbations are correlated (Kaiser 1987). Similarly, the redshift-space bispectrum depends on the line-of-sight projections μ_1 and μ_2 of $\boldsymbol{k}_1$ and $\boldsymbol{k}_2$ (as $\boldsymbol{k}_3=-\boldsymbol{k}_1-\boldsymbol{k}_2$). Therefore, the bispectrum depends on five variables, three of which determine the shape of the triangle of wavevectors while the remaining two indicate its orientation with respect to the line of sight. In Appendix A, we discuss two different parametrizations of the coefficients μ_1 and μ_2 in terms of convenient angular variables that here we schematically denote by $0\leq\theta\leq\pi$ and $0\leq\phi<2\pi$.

To reduce the complexity of cosmological investigations, the μ-dependence of the galaxy power spectrum at fixed wavenumber is often expanded in a Fourier–Legendre series (Taylor & Hamilton 1996)

$$P(\boldsymbol{k})=\sum_{\ell=0}^{\infty}P_\ell(k)\,\mathcal{L}_\ell(\mu)\,, \tag{9}$$

where $\mathcal{L}_\ell(\mu)$ denotes the Legendre polynomials and the functions

$$P_\ell(k)=\frac{2\ell+1}{2}\int_{-1}^{1}P(k)\,\mathcal{L}_\ell(\mu)\,{\rm d}\mu \tag{10}$$

are known as the 'redshift-space multipoles' of the power spectrum. In linear perturbation theory, only the monopole ($\ell=0$), quadrupole ($\ell=2$), and hexadecapole ($\ell=4$) do not vanish (see equation 18 in Section 2.3 without the exponential term on the rhs). Recent studies show that these three multipoles indeed contain the bulk of the information on the main cosmological parameters (e.g. Taruya, Saito & Nishimichi 2011; Kazin, Sánchez & Blanton 2012; Beutler et al. 2014). Therefore, a simplified inference method (with small information loss) can be engineered by only considering three functions of k instead of a function of both k and μ. This approach can be generalized to the galaxy bispectrum. In fact, the dependence on the orientation of a triangle of wavevectors can be decomposed into spherical harmonics (Scoccimarro, Couchman & Frieman 1999a),

$$B(\boldsymbol{k}_1,\boldsymbol{k}_2,\boldsymbol{k}_3)=\sum_{\ell=0}^{\infty}\sum_{m=-\ell}^{\ell}B_{\ell m}(k_1,k_2,k_3)\,Y_{\ell m}(\theta,\phi)\,, \tag{11}$$

where

$$B_{\ell m}(k_1,k_2,k_3)=\int_{-1}^{+1}\int_{0}^{2\pi}B(\boldsymbol{k}_1,\boldsymbol{k}_2,\boldsymbol{k}_3)\,Y^*_{\ell m}(\theta,\phi)\,{\rm d}\cos(\theta)\,{\rm d}\phi\,. \tag{12}$$

A popular choice is to focus on the coefficients with $m=0$ which are often called the 'redshift-space multipoles' of the bispectrum. They satisfy a relation similar to equation (9) for the ϕ-averaged bispectrum:

$$\int_0^{2\pi}B(\boldsymbol{k}_1,\boldsymbol{k}_2,\boldsymbol{k}_3)\,\frac{{\rm d}\phi}{2\pi}=\sum_{\ell=0}^{\infty}B_{\ell0}(k_1,k_2,k_3)\,\mathcal{L}_\ell(\cos\theta)\,. \tag{13}$$

These multipoles are simple to estimate from a galaxy catalogue using fast Fourier transform-based methods (Scoccimarro 2015, see also Bianchi et al. 2015) and provide a convenient procedure to compress the bispectrum measurements into data structures of lower dimensionality. This, however, unavoidably causes loss of information. For a fixed cosmological model, Gagrani & Samushia (2017) show that constraints on the velocity linear growth factor, galaxy bias coefficients and Alcock–Paczinsky parameters based on B_{00}, B_{20}, and B_{40} are quite similar to those derived from the full $(\theta,\,\phi)$ dependence of the bispectrum. This suggests that using only the lowest-order bispectrum multipoles is not associated with a significant loss of information about (at least) some selected cosmological parameters. We will revisit this issue using our own results in Section 5.3.

For the sake of completeness, in this work, we do not compress $P(\boldsymbol{k})$ and $B(\boldsymbol{k}_1,\boldsymbol{k}_2,\boldsymbol{k}_3)$ into their low-order multipoles and exploit their full angular dependence in redshift space. The price we pay for doing this is dealing with large data sets and high-dimensional covariance matrices.

2.3 Perturbative models

We model the galaxy power spectrum and the bispectrum in redshift space by combining three ingredients: (i) Standard Perturbation Theory (SPT) for the growth of long-wavelength density and velocity perturbations in a single-stream collisionless fluid (see Bernardeau et al. 2002 for a review), (ii) a galaxy bias model, and (iii) a non-perturbative phenomenological model for RSD due to motions within virialized structures ('finger-of-God' effect). We only consider expressions to the lowest non-vanishing order in the perturbations.

2.3.1 *Definitions*

We consider a flat Friedmann–Lemaître–Robertson–Walker (FLRW) background with expansion factor a and Hubble parameter H. The present-day value of H is $H_0 = 100\,h$ km s^{-1} Mpc^{-1}. We model dark energy as a barotropic fluid with equation of state $p = w\rho c^2$ where p and ρc^2 denote pressure and energy density, respectively, and w is a dimensionless parameter that can, in principle, change with a.

The evolution of a and H is regulated by Friedmann equations that can be expressed in terms of the present-day value of the matter density parameter $\Omega_{\rm m}$ and the dark-energy equation of state. Neglecting the late-time contribution from radiation, we have

$$\frac{H^2}{H_0^2} = \left(\frac{\Omega_{\rm m}}{a^3} + (1-\Omega_{\rm m})\,\exp\left\{-3\int_1^a [1+w(x)]\,{\rm d}\ln x\right\}\right)\,, \tag{14}$$

and the condition for the accelerated expansion of the Universe is $w < -1/3$.

On sub-horizon scales, linear density perturbations in the matter component grow proportionally to the growth factor D_+ that we compute by solving the ordinary differential equation

$$D_+'' + \left(\frac{3}{a} + \frac{{\rm d}\ln H}{{\rm d}\,a}\right) D_+' - \frac{3\Omega_{\rm m}}{2a^5\,(H^2/H_0^2)}\,D_+ = 0\,, \tag{15}$$

where the symbol $'$ denotes a derivative with respect to a. In order to link linear density and velocity perturbations, we introduce the growth-of-structure parameter

$$f = \frac{{\rm d}\ln D_+}{{\rm d}\ln a}\,. \tag{16}$$

2.3.2 *Galaxy biasing*

We adopt an Eulerian non-linear and non-local bias model to express the fluctuations in the galaxy density in terms of the underlying matter perturbations, $\delta(\boldsymbol{x})$, and the traceless tidal field with Cartesian components $s_{ij}(\boldsymbol{x}) = (\partial_i\partial_j - \delta_{ij}\,\nabla^2/3)\,\phi(\boldsymbol{x})$ (where δ_{ij} denotes the Kronecker symbol and the gravitational potential, $\phi(\boldsymbol{x})$, satisfies the Poisson equation $\nabla^2\phi = \delta$). Namely, we write

$$\delta_g(\boldsymbol{x}) = b_1\,\delta(\boldsymbol{x}) + \frac{b_2}{2}\left[\delta^2(\boldsymbol{x}) - \langle\delta^2(\boldsymbol{x})\rangle\right] + \frac{b_{s^2}}{2}\left[s^2(\boldsymbol{x}) - \langle s^2(\boldsymbol{x})\rangle\right]\,, \tag{17}$$

where b_1, b_2, and b_{s^2} denote the linear, the non-linear, and the tidal (non-local) bias parameters, respectively. Equation (17) extends the local bias model introduced by Fry & Gaztanaga (1993) to account for the anisotropy and environmental dependence of gravitational collapse (Catelan et al. 1998). The tidal-bias term alters the dependence of the galaxy bispectrum on the triangular configurations of the wavevectors (Catelan, Porciani & Kamionkowski 2000) and a non-vanishing b_{s^2} has been measured for dark-matter haloes extracted from cosmological simulations (Baldauf et al. 2012; Chan, Scoccimarro & Sheth 2012; Saito et al. 2014; Bel, Hoffmann & Gaztañaga 2015). The tidal bias is also required to ensure a proper renormalization (in the field-theory sense) of the quadratic local bias that is otherwise sensitive to short-wavelength modes of the density field that are not suitable for a perturbative analysis (McDonald & Roy 2009; Assassi et al. 2014; Desjacques, Jeong & Schmidt 2018).

Equation (17) is nowadays the standard bias model for the galaxy bispectrum and is routinely used to interpret observational data (Gil-Marín et al. 2015, 2017) and make forecasts for future missions (Tellarini et al. 2016; Karagiannis et al. 2018; Moradinezhad Dizgah et al. 2018).

2.3.3 *Galaxy power spectrum and bispectrum*

We only consider expressions to the lowest non-vanishing order in the perturbations corrected with a phenomenological model for non-linear RSD. For the galaxy power spectrum in redshift space we thus write

$$P(\boldsymbol{k}) = Z_1^2(\boldsymbol{k})\,P_{\rm L}(k)\,\exp\left[-\frac{(k\,\mu\,\sigma_{\rm p})^2}{2}\right]\,, \tag{18}$$

where $P_{\rm L}$ is the power spectrum of linear matter-density fluctuations and

$$Z_1(\boldsymbol{k}) = Z_1(k,\mu) = b_1 + f\mu^2 \tag{19}$$

accounts for linear biasing and linear RSD. The exponential term, instead, provides a phenomenological (non-perturbative) characterization of the suppression of power due to non-linear velocities. It describes virialized motions as an incoherent Gaussian scatter with (scale-independent) pairwise velocity dispersion $a\,H\,\sigma_{\rm p}$ (here $\sigma_{\rm p}$ is conveniently expressed in units of h^{-1} Mpc) and it has been shown to approximately match the results of N-body simulations when $\sigma_{\rm p}$ is treated as a free parameter (Peacock 1992; Peacock & Dodds 1994; Ballinger, Peacock & Heavens 1996). Note that $a\,H\,\sigma_{\rm p}$ does not coincide with the actual pairwise velocity dispersion of the galaxies (which is scale-dependent, e.g. Scoccimarro 2004; Kuruvilla & Porciani 2018) and should be merely considered as a nuisance parameter of the same order of magnitude. It is also important to stress that, at the scales analysed in this work, the exponential term in equation (18) is always very close to unity and can be approximated as $1-(k\,\mu\,\sigma_{\rm p})^2/2$. Therefore, our results do not depend on the assumption of a Gaussian (rather than a Lorentzian) damping factor.

Similarly, for the galaxy bispectrum, we get

$$B(\boldsymbol{k}_1,\boldsymbol{k}_2,\boldsymbol{k}_3) = 2\left[Z_2(\boldsymbol{k}_1,\boldsymbol{k}_2)\,Z_1(\boldsymbol{k}_1)\,Z_1(\boldsymbol{k}_2)\,P_{\rm L}(k_1)P_{\rm L}(k_2) + {\rm cycl.}\right] \times \exp\left[-(k_1^2\mu_1^2 + k_2^2\mu_2^2 + k_3^2\mu_3^2)\,\frac{\sigma_{\rm p}^2}{2}\right]\,, \tag{20}$$

where the cyclic permutation runs over pairs of $\boldsymbol{k}_1$, $\boldsymbol{k}_2$, and $\boldsymbol{k}_3$ and the second-order kernel describing the effect of non-linearities due to dynamics, biasing and RSD is

$$Z_2(\boldsymbol{k}_i,\boldsymbol{k}_j) = \frac{b_2}{2} + b_1 F_2(\boldsymbol{k}_i,\boldsymbol{k}_j) + f\mu_{ij}^2 G_2(\boldsymbol{k}_i,\boldsymbol{k}_j) + \frac{f\,\mu_{ij}k_{ij}}{2}\left[\frac{\mu_i}{k_i}Z_1(\boldsymbol{k}_j) + \frac{\mu_j}{k_j}Z_1(\boldsymbol{k}_i)\right] + \frac{b_{s^2}}{2}S_2(\boldsymbol{k}_i,\boldsymbol{k}_j)\,. \tag{21}$$

Here, $\boldsymbol{k}_{ij} = \boldsymbol{k}_i + \boldsymbol{k}_j$ and $\mu_{ij} = \boldsymbol{k}_{ij}\cdot\hat{\boldsymbol{s}}/k_{ij}$, while F_2 and G_2 denote the second-order kernels of the density and the velocity fields, respectively,

$$F_2(\boldsymbol{k}_i,\boldsymbol{k}_j) = \frac{5}{7} + \frac{m_{ij}}{2}\left(\frac{k_i}{k_j} + \frac{k_j}{k_i}\right) + \frac{2}{7}\,m_{ij}^2\,, \tag{22}$$

$$G_2(\boldsymbol{k}_i,\boldsymbol{k}_j) = \frac{3}{7} + \frac{m_{ij}}{2}\left(\frac{k_i}{k_j} + \frac{k_j}{k_i}\right) + \frac{4}{7}\,m_{ij}^2\,, \tag{23}$$

where $m_{ij} = \left(\boldsymbol{k}_i\cdot\boldsymbol{k}_j\right)/\left(k_i k_j\right)$. Finally, the tidal kernel

$$S_2(\boldsymbol{k}_i,\boldsymbol{k}_j) = m_{ij}^2 - \frac{1}{3}. \tag{24}$$

Although equations (22) and (23) hold true only in an Einstein-de Sitter universe, they provide accurate approximations in the general case (Scoccimarro et al. 1998; Bernardeau et al. 2002; Fonseca de la Bella et al. 2017). Consistently with the power-spectrum analysis, in equation (20), we adopt a Gaussian damping function to describe non-perturbative contributions to RSD. This term depends on the parameter $\sigma_{\rm p}$ that we also use for the power spectrum. Tests conducted against N-body simulations show that this is a reasonable approximation for matter clustering on sufficiently large scales and for redshifts $z > 0.5$ (Hashimoto, Rasera & Taruya 2017). In this case, the best-fitting $\sigma_{\rm p}$ does not differ much from linear-theory predictions.

2.4 Discreteness effects

Galaxies are discrete objects and their clustering statistics are affected by shot noise. Assuming that their distribution derives from Poisson sampling an underlying continuous density field allows us to relate the observed spectra (denoted with a tilde) with those given in equations (18) and (20) (e.g. Matarrese et al. 1997). In terms of the galaxy number density, $n_{\rm g}$,

$$\tilde{P}(\boldsymbol{k}) = P(\boldsymbol{k}) + P_{\rm shot}\ , \tag{25}$$

$$\begin{aligned}\tilde{B}(\boldsymbol{k}_1,\boldsymbol{k}_2,\boldsymbol{k}_3) &= B(\boldsymbol{k}_1,\boldsymbol{k}_2,\boldsymbol{k}_3) \\ &+ [P(\boldsymbol{k}_1)+P(\boldsymbol{k}_2)+P(\boldsymbol{k}_3)]\,P'_{\rm shot} + B_{\rm shot}\ ,\end{aligned} \tag{26}$$

where $P_{\rm shot} = P'_{\rm shot} = n_{\rm g}^{-1}$ and $B_{\rm shot} = n_{\rm g}^{-2}$.

3 FISHER MATRIX

3.1 Estimators and finite-volume effects

Actual redshift surveys cover finite comoving volumes and contain observational artefacts (gaps, masked regions, variable depth, etc.). Clustering statistics are thus measured using specifically designed estimators that minimize the impact of these features. An estimate for $\delta_{\rm g}(\boldsymbol{x})$ is usually computed by weighing the contribution of each galaxy based on the selection criteria of the survey (Feldman, Kaiser & Peacock 1994). Schematically, the observed galaxy overdensity can be written as $\delta_{\rm obs}(\boldsymbol{x}) = \delta_{\rm g}(\boldsymbol{x})\,W(\boldsymbol{x})$ (where $W(\boldsymbol{x})$ is the window function of the survey) so that $\tilde{\delta}_{\rm obs}(\boldsymbol{k}) = \int \tilde{W}(\boldsymbol{q})\,\tilde{\delta}_{\rm g}(\boldsymbol{k}-\boldsymbol{q})\,{\rm d}^3q/(2\pi)^3$. Therefore, an estimator for the power spectrum in redshift space can be built by replacing the ensemble average in equation (4) with a mean taken over a finite bin of wavevectors with similar values of k and μ in a single realization:

$$\hat{P}_i = V^{-1}\int_{\mathcal{K}_i} \tilde{\delta}_{\rm obs}(\boldsymbol{k})\,\tilde{\delta}_{\rm obs}(-\boldsymbol{k})\,\frac{{\rm d}^3k}{K_{\rm s}}\ . \tag{27}$$

Here, $V = \int W(\boldsymbol{x})\,{\rm d}^3x$ denotes the effective volume of the survey and $K_{\rm s}$ is the k-space volume covered by the bin $\boldsymbol{k}\in\mathcal{K}_i$. The ensemble average of $\hat{P}_i$ is

$$\langle\hat{P}_i\rangle = \int \tilde{W}(\boldsymbol{k}_i-\boldsymbol{q})\,P(\boldsymbol{q})\,\frac{{\rm d}^3q}{(2\pi)^3} + \text{shot noise terms}, \tag{28}$$

and thus $\hat{P}_i$ is a biased estimator. This reflects the fact that plane waves (the basis functions of the Fourier expansion) are not orthonormal over a finite, non-periodic volume. Typically, $\tilde{W}(\boldsymbol{k})$ shows a prominent peak at $\boldsymbol{k}\simeq 0$ with a width of $\Delta k \sim V^{-1/3}$ (if the surveyed volume is not elongated, otherwise Δk coincides with the inverse of the shortest dimension). Therefore, the power-spectrum estimator in equation (27) mixes the contributions from Fourier modes with wavenumber differences $\Delta k < V^{-1/3}$. This is a manifestation of the uncertainty principle between conjugate variables in a Fourier transform: if the galaxy positions are confined to a region of linear size $V^{1/3}$, then the wavenumbers of the Fourier modes are 'uncertain' within a range $2\pi/V^{1/3}$.

Likewise, after introducing an estimator for the bispectrum that averages over a set of triangular configurations $\mathcal{T}_i$ centred around $(\boldsymbol{k}_1,\boldsymbol{k}_2,-\boldsymbol{k}_1-\boldsymbol{k}_2)$

$$\hat{B}_i = V^{-1}\int_{\mathcal{T}_i} \tilde{\delta}_{\rm obs}(\boldsymbol{p})\,\tilde{\delta}_{\rm obs}(\boldsymbol{q})\,\tilde{\delta}_{\rm obs}(-\boldsymbol{p}-\boldsymbol{q})\,\frac{{\rm d}^3p\,{\rm d}^3q}{K_\triangle} \tag{29}$$

with

$$K_\triangle = \int_{\mathcal{T}_i} \delta_{\rm D}(\boldsymbol{p}+\boldsymbol{q}+\boldsymbol{k})\,{\rm d}^3p\,{\rm d}^3q\,{\rm d}^3k\ , \tag{30}$$

(Scoccimarro 2000) one finds (e.g. Gil-Marín et al. 2015)

$$\begin{aligned}\langle\hat{B}_i\rangle = &\int \tilde{W}(\boldsymbol{k}_1-\boldsymbol{q})\,\tilde{W}(\boldsymbol{k}_2-\boldsymbol{q})\,B(\boldsymbol{q}_1,\boldsymbol{q}_2,-\boldsymbol{q}_1-\boldsymbol{q}_2)\,\frac{{\rm d}^3q_1}{(2\pi)^3}\,\frac{{\rm d}^3q_2}{(2\pi)^3} \\ &+\text{shot noise terms}.\end{aligned} \tag{31}$$

Although the systematic shift of $\hat{P}_i$ and $\hat{B}_j$ due to the window function is only noticeable on scales comparable with the extension of the survey, it needs to be accounted for in order to make unbiased inference about the cosmological parameters. One option is to deconvolve the window function from the measured spectra (Lucy 1974; Baugh & Efstathiou 1993; Lin et al. 1996). Alternatively, the theoretical models can be convolved with the window function of the survey before performing a fit to the measured spectra. A third possibility is not to use the Fourier decomposition and expand the galaxy density in orthonormal modes that maximize the signal-to-noise ratio (S/N) given the survey geometry and the selection function (plus a fiducial model for the spectra) using the Karhunen–Loève transform (Vogeley & Szalay 1996; Tegmark, Taylor & Heavens 1997).

For simplicity, in this work, we only approximately take into account the effects of the window function by considering k-bins of size $\Delta k = 2\pi/V^{1/3} = k_{\rm f}$ (i.e. the expected broadening for the primary peak[1] of $\tilde{W}$ for a cubic survey volume of side $L = V^{1/3}$). We thus compute the band-averaged power spectra and bispectra by evaluating the mean over the set of configurations that contribute to each bin. Note that most forecast papers instead just use one characteristic configuration per bin to speed the calculation up.

3.2 Binning strategy and covariance matrices

3.2.1 Power spectrum

Within the distant-observer approximation, the galaxy power spectrum in redshift space is a function of k and μ^2. Therefore, we define our power-spectrum estimator using bins that run over a spherical shell of Fourier modes of widths Δk and $\Delta\mu$ and central values $\bar{k}_i$ and $\bar{\mu}_i$. In this case,

$$K_s = \int_{\mathcal{K}_i} {\rm d}^3q = 2\pi\,\Delta\mu\left[\bar{k}^2\Delta k + \frac{(\Delta k)^3}{12}\right] \simeq 2\pi\,\Delta\mu\,\bar{k}_i^2\,\Delta k, \tag{32}$$

[1]If $W(\boldsymbol{x}) = 1$ within a cube of side L and 0 otherwise, then $\tilde{W}(\boldsymbol{k}) = \prod_{i=1}^3 (2/k_i)\,\sin(k_i\,L/2)$ and the main peak along each Cartesian component extends for $\Delta k = 2\pi/L$ on the positive-frequency side.

where the last expression on the right-hand side is valid only for narrow bins with $\Delta k \ll \bar{k}_i$. Note that the estimator in equation (27) is symmetric between $\boldsymbol{k}$ and $-\boldsymbol{k}$ meaning that, for every $\bar{k}_i$, it suffices to consider the interval $0 \leq \mu \leq 1$ and partition it over the bins of size $\Delta\mu$.

The covariance matrix of an estimator encodes information regarding the precision to which the estimand can be measured and the correlations between estimates corresponding to different configurations. The covariance matrix for the binned galaxy power spectrum is defined as

$$(C_{\rm PP})_{ij} = \langle (\hat{P}_i - \langle \hat{P}_i \rangle)(\hat{P}_j - \langle \hat{P}_j \rangle) \rangle = \langle \hat{P}_i\, \hat{P}_j \rangle - \langle \hat{P}_i \rangle \langle \hat{P}_j \rangle \qquad (33)$$

and it can be decomposed in a disconnected (or Gaussian, since it is the only term present for a Gaussian random field) contribution and a connected (or non-Gaussian) contribution that is proportional to the trispectrum (the Fourier transform of the connected 4-point correlation function) of the galaxy distribution. On the large scales, we are interested in, the Gaussian contribution dominates (Scoccimarro, Zaldarriaga & Hui 1999b; Bertolini et al. 2016; Mohammed, Seljak & Vlah 2017) and, for narrow bins, we can write (Feldman et al. 1994; Meiksin & White 1999)

$$(C_{\rm PP})_{ij} \simeq \frac{2\,\tilde{P}_i^2}{N_{\rm P}}\,\delta_{ij}\ , \qquad (34)$$

where

$$N_{\rm P} = \frac{K_s}{k_{\rm f}^3} \simeq \frac{V}{(2\pi)^2}\,\bar{k}_i^2\,\Delta k\,\Delta\mu\ . \qquad (35)$$

The ratio $N_{\rm P}/2$ gives the number of independent fundamental Fourier cells contributing to the band averaged power spectrum. The 2 at the denominator comes from the fact that the density field is real valued and $\tilde{\delta}(-\boldsymbol{k}) = \tilde{\delta}(\boldsymbol{k})^*$. Note that the statistical noise of $\hat{P}_i$ reflects the survey size: larger surveys contain more independent Fourier modes that contribute to a given bin and thus are associated with smaller random errors. Strictly speaking, equation (34) is exact only for cubic volumes with periodic boundary conditions but it is reasonable to expect that, to first approximation, the covariance does not depend on the survey shape (especially for $k \gg k_{\rm f}$). It is also worth mentioning that only the Gaussian part of $C_{\rm PP}$ is diagonal and non-linear couplings between Fourier modes generate non-vanishing off-diagonal terms.

3.2.2 *Bispectrum*

The galaxy bispectrum in redshift space depends on the triangular configuration of the wavevectors and its orientation with respect to the line of sight. In this section, we show that the orientation dependence severely complicates the analysis with respect to studies of the bispectrum in real space or the monopole in redshift space.

We characterize the shape of a triangle using an ordered triplet of numbers that indicate the length of its sides: $k_{\rm s} \leq k_{\rm m} \leq k_{\rm l}$. To describe its orientation, we need to use two angular variables that, for the moment, we denote using a generic solid angle Ω. Therefore, we define our bispectrum estimator using finite bins with central values $\bar{k}_{\rm s}, \bar{k}_{\rm m}, \bar{k}_{\rm l}, \bar{\Omega}$ as well as widths $\Delta k_{\rm s} = \Delta k_{\rm m} = \Delta k_{\rm l} = \Delta k$ and $\Delta\Omega$. It follows that,

$$K_{\triangle} \simeq 8\pi^2\,\bar{k}_{\rm l}\,\bar{k}_{\rm m}\,\bar{k}_{\rm s}\,(\Delta k)^3\,\Sigma(\bar{\Omega})\,\Delta\Omega\ , \qquad (36)$$

where $\Sigma(\bar{\Omega})\,\Delta\Omega$ denotes the fraction of triangles with fixed shape that populate a bin with solid angle $\Delta\Omega$, i.e. $\int_{4\pi} \Sigma(\Omega)\,{\rm d}\Omega = 1$. Note that the right-hand side of equation (36) should be divided by 2 for degenerate triangular configurations contained in a line (Mehrem 2009; Chan & Blot 2017).

We now discuss more in detail how to parametrize the orientation of a triangle with respect to the line of sight. To this end, in Appendix A, we introduce two different coordinate systems that we dub (ω, χ) and (θ, ϕ). They both define spherical coordinates but use different polar axes: the triangle's normal for (ω, χ) and one of the legs of the triangle for (θ, ϕ). A third possibility that more closely matches power-spectrum studies is to directly use μ_1 and μ_2 as indicators of the orientation of the triangle (e.g. Song et al. 2015). We briefly discuss here advantages and disadvantages of these three options. In the left column of Fig. 1, we show how RSD modify the shot-noise-subtracted galaxy bispectrum for a fixed triangular configuration. From top to bottom, we show the ratio between the redshift-space bispectrum and its real-space counterpart as a function of (ω, χ), (θ, ϕ), and (μ_1, μ_2). Note that, for selected orientations, RSD enhances the clustering signal by more than an order of magnitude. Obviously, the size of the distortions is the same in all panels but their overall pattern appears very different in the various coordinate systems that are connected by non-linear transformations.

Another important quantity to analyse is the function $\Sigma(\Omega)$ that determines the noise of the bispectrum estimator as a function of the orientation of the triangles. By construction, the number of triangles are uniformly distributed in $\mathrm{d}\cos\omega\,\mathrm{d}\chi$ and $\mathrm{d}\cos\theta\,\mathrm{d}\phi$, i.e. $\Sigma(\omega, \chi) = (4\pi)^{-1}\sin\omega$ and $\Sigma(\theta, \phi) = (4\pi)^{-1}\sin\theta$. On the other hand, the distribution of orientations gets more complicated when expressed in terms of the (μ_1, μ_2) coordinates. Using equations (A7) and (A8) to evaluate the Jacobian determinant of the coordinate transformation, we obtain[2]

$$\Sigma(\mu_1, \mu_2) = \left(2\pi\sqrt{\sin^2\xi_{12} - \mu_1^2 - \mu_2^2 + 2\cos\xi_{12}\,\mu_1\mu_2}\right)^{-1}\ . \qquad (37)$$

The results of a Monte Carlo simulation obtained by randomly rotating the same triangle confirm our analytical results (the bottom right-hand panel in Fig. 1). Triangles only populate a finite region of the (μ_1, μ_2) plane bounded by an ellipse whose orientation depends on the shape of the triangles as defined by the shortest rotation angle ξ_{12} between $\boldsymbol{k}_1$ and $\boldsymbol{k}_2$. The density of triangles increases considerably towards the boundaries of the ellipse. Regrettably, this subtlety has been missed by Song et al. (2015) who, in their equation (20), assume that triangles are uniformly distributed within the entire (μ_1, μ_2) plane. Therefore, some care should be taken when interpreting their forecasts.

In the left column of Fig. 1, the symmetry between the triangles $(\boldsymbol{k}_1, \boldsymbol{k}_2, \boldsymbol{k}_3)$ and $(-\boldsymbol{k}_1, -\boldsymbol{k}_2, -\boldsymbol{k}_3)$ is evident. This corresponds to the transformations $(\omega, \chi) \to (\omega, \pi + \chi)$, $(\theta, \phi) \to (\pi - \theta, 2\pi - \phi)$, and $(\mu_1, \mu_2) \to (-\mu_1, -\mu_2)$. In practical applications, it makes sense, then, to select bins that combine these two configurations so that to reduce the size of the data and, as we are about to show, also get a diagonal covariance matrix (to first approximation). Moreover, RSD also possess an additional symmetry due to the fact that they only depend on $\sin\omega$ or $\sin\phi$. It is possible to 'fold' the original coordinate systems (ω, χ) and (θ, ϕ) so that to optimally exploit all these symmetries. We separately discuss how to do this in Section A4 so as not to interrupt the flow of the discussion with technicalities. Here, it suffices to say that we end

[2]Since μ_2 only depends on $\sin\phi$, there are two values of ϕ that give the same μ_2. This explains the factor 2π in equation (37).

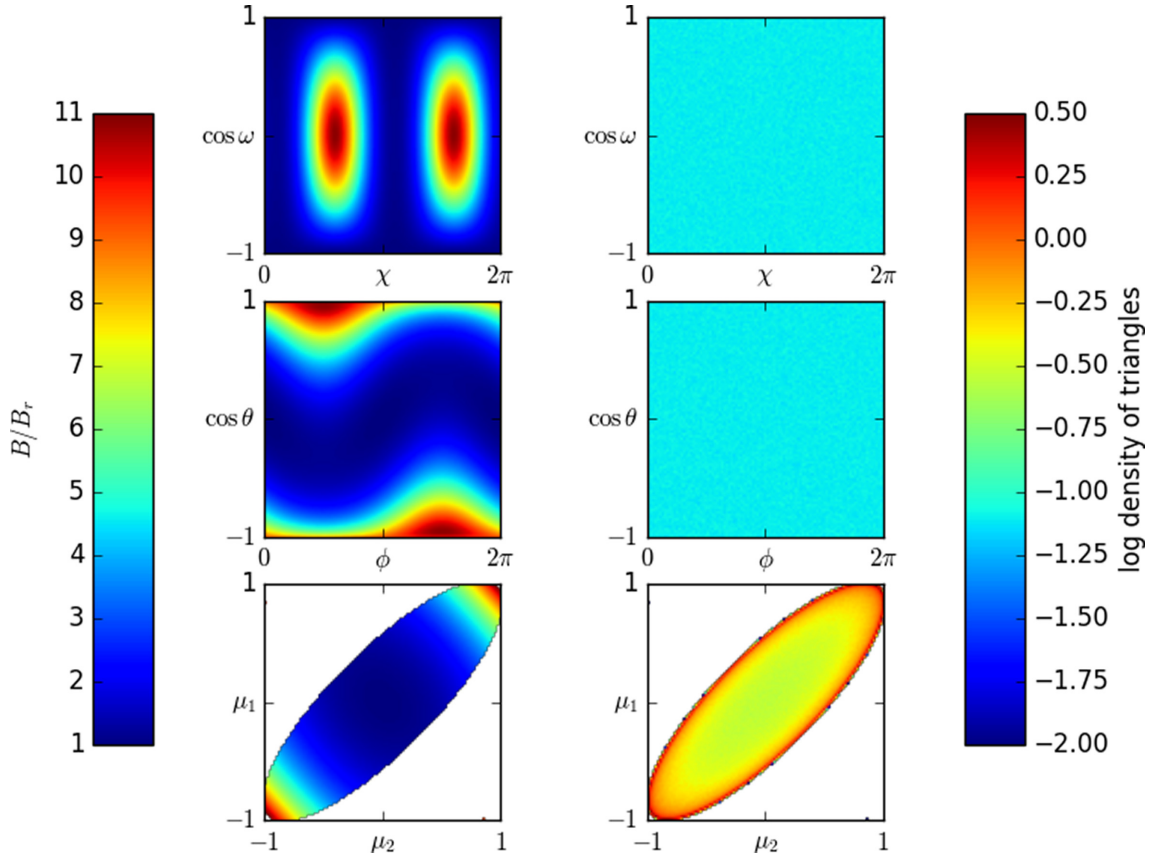

Figure 1. The panels on the left-hand side illustrate an example of how RSD affect the bispectrum. Shown is the ratio between the redshift-space and real-space bispectrum for a fixed triangular configuration of wavevectors with $(k_1, k_2, k_3) = (23, 14, 10) \times 3.93 \times 10^{-3}\, h$ Mpc^{-1}. From top to bottom, three different coordinate systems are used to parametrize the relative orientation of the triangle and the line of sight (see the main text and Appendix A for details). The corresponding probability density of finding a triangle with a given orientation is shown in the right-hand-side panels.

up using two sets of variables, $(\tilde{\omega}, \tilde{\chi})$ or $(\tilde{\theta}, \tilde{\phi})$, with the following range of variability: $0 \leq \tilde{\omega} < \pi/2$, $0 \leq \tilde{\chi} < \pi$, $0 \leq \tilde{\theta} < \pi/2$, and $\pi/2 \leq \tilde{\phi} < 3\pi/2$. Although they span a more compact range, the new coordinates fully cover the original parameter space shown in Fig. 1. The left column of Fig. 2 illustrates how they optimally isolate the basic pattern that repeats four times in Fig. 1. It is also worth stressing that random triangular orientations are still uniformly distributed in terms of the variables $(\cos\tilde{\omega}, \tilde{\chi})$ and $(\cos\tilde{\theta}, \tilde{\phi})$. For this reason, we partition parameter space into $N_\mathrm{p} \times N_\mathrm{a}$ identical bins of linear size $1/N_\mathrm{p}$ for the cosine of the polar angle (i.e. $\cos\tilde{\omega}$ or $\cos\tilde{\theta}$) and π/N_a for the azimuthal angle (i.e. $\tilde{\chi}$ or $\tilde{\phi}$). The right column of Fig. 2 shows an example of how RSD look like when $N_\mathrm{p} = 4$ and $N_\mathrm{a} = 3$.

The covariance matrix for the bispectrum estimator is

$$(C_{\mathrm{BB}})_{ij} = \langle (\hat{B}_i - \langle \hat{B}_i \rangle)(\hat{B}_j - \langle \hat{B}_j \rangle) \rangle = \langle \hat{B}_i\, \hat{B}_j \rangle - \langle \hat{B}_i \rangle \langle \hat{B}_j \rangle \ , \quad (38)$$

where the indices i and j label bins of triangular configurations and orientations for the wavevectors. Also in this case, the covariance can be decomposed into Gaussian and non-Gaussian contributions that include terms up to the pentaspectrum (i.e. the Fourier transform of the connected six-point correlation function). The Gaussian part (which is expected to dominate on large scales) receives non-vanishing contributions whenever any one of the sides of the triangle i is the opposite vector to any one of the sides of the triangle j. Therefore, if the bispectrum bins are chosen such that a triangle and its

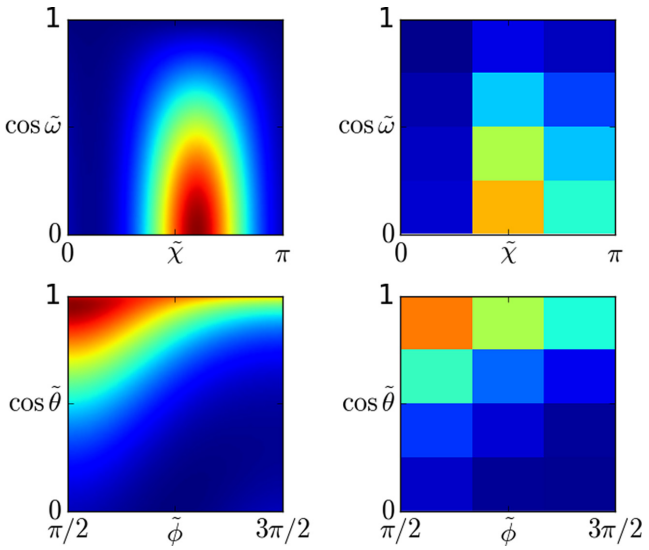

Figure 2. The RSD displayed in Fig. 1 are now plotted as a function of the optimal angular coordinates $(\tilde{\omega}, \tilde{\chi})$ and $(\tilde{\theta}, \tilde{\phi})$. We adopt infinite resolution in the left-hand-side panels and partition parameter space into 12 bins in the right-hand-side panels. The colour coding is the same as in Fig. 1.

negative end up in the same bin, we obtain (Fry, Melott & Shandarin 1993; Scoccimarro et al. 2004; Sefusatti et al. 2006; Chan & Blot 2017)

$$(C_{\rm BB})_{ij} \simeq \frac{s_{\rm B}\, V\, \tilde{P}_{i\rm l}\, \tilde{P}_{i\rm m}\, \tilde{P}_{i\rm s}}{N_B}\, \delta_{ij}\ , \tag{39}$$

where the indices (*i*l, *i*m, *i*s) identify the lengths and orientations of the sides of the triangular configuration $\triangle_i$ and

$$N_B \simeq \frac{K_\triangle}{k_{\rm f}^6} \simeq \frac{V^2}{8\pi^4}\, \bar{k}_{\rm l}\, \bar{k}_{\rm m}\, \bar{k}_{\rm s}\, (\Delta k)^3\, \Sigma(\bar{\Omega})\, \Delta\Omega \tag{40}$$

gives the number of triangles falling into a bin for shapes and orientations and the coefficient $s_{\rm B} = 6, 2, 1$ for equilateral, isosceles, and scalene bin configurations, respectively. This number counts the matching pairs between the sides of the bins $\triangle_i$ and $\triangle_j$. Note that the diagonal elements of the covariance matrix are inversely proportional to the survey volume.

Finally, we consider the (rectangular) cross-covariance matrix between the estimators for the power spectrum and the bispectrum,

$$(C_{\rm PB})_{ij} = \langle (\hat{P}_i - \langle \hat{P}_i \rangle)(\hat{B}_j - \langle \hat{B}_j \rangle) \rangle = \langle \hat{P}_i\, \hat{B}_j \rangle - \langle \hat{P}_i \rangle\, \langle \hat{B}_j \rangle \tag{41}$$

which is composed of a disconnected part proportional to the product between P and B and a connected part proportional to the quadrispectrum (the Fourier transform of the connected 5-point correlation function). Sefusatti et al. (2006) report that, although this quantity does not have a Gaussian contribution, it is non-negligible even on large scales where the disconnected part dominates. In order to evaluate this term for our binning scheme, we need to generalize the expressions found in the literature that do not consider the orientation of the triangles. A non-vanishing cross-covariance is generated by configurations in which the wavevector $\boldsymbol{k}$ in the power-spectrum estimator, equation (27), coincides with (or with the reverse of) one of the legs $\boldsymbol{p}$, $\boldsymbol{q}$, and $-\boldsymbol{p}-\boldsymbol{q}$ of the triangle in the bispectrum estimator, equation (29). When the bins for the power spectrum ($\boldsymbol{k} \in \mathcal{K}_i$) and for the legs of the bispectrum triangles, $(\boldsymbol{p}, \boldsymbol{q}, -\boldsymbol{p}-\boldsymbol{q}) \in \mathcal{T}_j$, are taken with the same criterion (for instance by only requiring that $\bar{k}_i - \Delta k/2 < k < \bar{k}_i + \Delta k/2$, so that the bispectrum estimator can be labelled with three indices $\hat{B}_{j_1 j_2 j_3}$) either zero or all triangles in $\mathcal{T}_{j_1 j_2 j_3}$ have, say, $\boldsymbol{q} \in \mathcal{K}_i$ and the cross-covariance between $\hat{P}_i$ and $\hat{B}_{j_1 j_2 j_3}$ is given by $(C_{\rm PB})_{ij} \simeq 2\, s_{\rm PB}\, \hat{P}_i\, \hat{B}_j\, (\delta_{ij_1} + \delta_{ij_2} + \delta_{ij_3})/N_P$ with $s_{\rm PB} = 3, 2, 1$ for equilateral, isosceles, and scalene triangles, respectively. However, to study the bispectrum in redshift space, we also bin in Ω and we need to take into account that $\mu_{\rm m}$ and $\mu_{\rm s}$ also depend on the angular variables. Because of this, the k-space volumes spanned by $\boldsymbol{k}_{\rm m}$ and $\boldsymbol{k}_{\rm s}$ within a triangular bin partially overlap with several power-spectrum bins. Let us denote by $I_{ij_\ell}/N_{\rm B}$ the fraction of triangles in $\mathcal{T}_j$ that have $\boldsymbol{k}_\ell \in \mathcal{K}_i$ (i.e. a bin for k_ℓ and μ_ℓ). Then,

$$(C_{\rm PB})_{ij} \simeq 2\, s_{\rm PB}\, \frac{\hat{P}_i\, \hat{B}_j}{N_{\rm P}\, N_{\rm B}}\, \left(I_{ij_1} + I_{ij_2} + I_{ij_3}\right). \tag{42}$$

Note that $\sum_i I_{ij} = N_{\rm B}$, where the sum is performed over all the bins for the power spectrum. For infinitesimally narrow bins, we can derive the coefficients I_{ij} analytically starting from equations (A5) and (A6) or (A7) and (A8). However, for the broad angular bins we consider in this work, we determine them numerically.

3.3 Survey characteristics and fiducial values

As an example of the forthcoming next generation of galaxy redshift surveys, we consider a *Euclid*-like mission. Within 6 yr starting from 2021, the *Euclid* space telescope is expected to complete a wide survey that will measure $\sim 6 \times 10^7$ galaxy redshifts over 15 000 deg^2 on the sky (Laureijs et al. 2011). Low-resolution (slitless) spectroscopy in the near infrared will target the emission lines (mainly H α) of star-forming galaxies in the approximate redshift interval $0.7 < z < 2.0$.

Table 1. Specifics of a *Euclid*-like survey in 14 non-overlapping redshift bins centred at z and of width $\Delta z = 0.1$. The comoving volume covered by the survey, V, the galaxy number density, $n_{\rm g}$, the characteristic halo mass, M_0, defined in equation (44), and the rescaled pairwise velocity dispersion, $\sigma_{\rm p}$, are expressed in units of h^{-3} Gpc^3, $10^{-3}\, h^3$ Mpc^{-3}, $10^{12} h^{-1} {\rm M}_\odot$, and h^{-1} Mpc, respectively.

z	V	$n_{\rm g}$	b_1	b_2	b_{s^2}	M_0	$\mathcal{N}_{\rm HO}$	$\sigma_{\rm p}$
0.7	2.82	2.76	1.18	−0.76	−0.10	1.04	0.455	4.81
0.8	3.28	2.04	1.22	−0.76	−0.13	0.96	0.315	4.72
0.9	3.70	1.53	1.26	−0.75	−0.15	0.88	0.220	4.62
1.0	4.08	1.16	1.30	−0.74	−0.17	0.81	0.156	4.51
1.1	4.42	0.88	1.34	−0.72	−0.19	0.73	0.108	4.39
1.2	4.72	0.68	1.38	−0.70	−0.22	0.67	0.078	4.27
1.3	4.98	0.52	1.42	−0.68	−0.24	0.60	0.055	4.15
1.4	5.20	0.38	1.46	−0.66	−0.26	0.55	0.037	4.03
1.5	5.38	0.26	1.50	−0.63	−0.29	0.49	0.023	3.92
1.6	5.54	0.20	1.54	−0.60	−0.31	0.45	0.017	3.81
1.7	5.67	0.15	1.58	−0.57	−0.33	0.41	0.012	3.70
1.8	5.77	0.11	1.62	−0.53	−0.35	0.37	0.008	3.61
1.9	5.85	0.09	1.66	−0.49	−0.38	0.33	0.006	3.49
2.0	5.92	0.07	1.70	−0.45	−0.40	0.30	0.004	3.40

Since only relatively small samples have been observed so far (for a summary see e.g. Pozzetti et al. 2016), little is known about the population of emission-line galaxies at these redshifts. Therefore, we must approximate the specifics of a *Euclid*-like survey by using theoretical models that have been calibrated against the current data. In particular, we adopt model 1 in Pozzetti et al. (2016) for the luminosity function of H α-selected galaxies and assume a limiting flux of $F_{{\rm H}\,\alpha} > 3 \times 10^{-16}$ erg cm^{-2} s^{-1}. In Table 1, we report the corresponding galaxy number densities, $n_{\rm g}$, as a function of redshift. In order to facilitate comparison with previous work, we adopt the same binning strategy as in the *Euclid* Definition Study Report (Laureijs et al. 2011) and in many other forecasts for this mission (e.g. Amendola et al. 2018): 14 non-overlapping redshift bins of width $\Delta z = 0.1$ whose central values are linearly spaced between 0.7 and 2.0.

The clustering properties of H α emitters at $z \sim 1$ are also very poorly constrained. Semi-analytic models of galaxy formation combined with N-body simulations suggest that the linear bias parameter of the emission-line galaxies that will be detected by *Euclid* should be slightly above unity at $z \sim 0.7$ and grow with redshift (Orsi et al. 2010). An approximate fit (that we adopt) for the effective linear bias in each redshift bin is $b_1 = 0.9 + 0.4\, z$ (see appendix A in Pozzetti et al. 2016), although observations over two degree-sized fields at slightly higher redshifts indicate that b_1 could be a bit higher ($b_1 = 2.4^{+0.1}_{-0.2}$ at $z = 2.23$, Geach et al. 2012). Determining realistic fiducial values for the quadratic and tidal bias coefficients of *Euclid* galaxies requires making some additional assumptions. It is a basic tenet of the standard cosmological model that galaxies lie within dark-matter haloes: a central galaxy sits in the densest region of a halo while multiple satellites can be found in the outskirts. The linear and quadratic bias coefficients of the host haloes depend on the halo mass and redshift but can be related to each other by using fitting functions calibrated against N-body simulations,

typically polynomials of second or third order (Lazeyras et al. 2016; Hoffmann, Bel & Gaztañaga 2017). Similarly, if halo formation is a local process in Lagrangian space and there is no initial tidal bias, then

$$b_{s^2} = \frac{4}{7}(1 - b_1) \tag{43}$$

(Catelan et al. 1998; Catelan et al. 2000; Baldauf et al. 2012; Chan et al. 2012). In brief, under some reasonable assumptions, knowing b_1 is sufficient to derive b_2 and b_{s^2} for the host haloes. In order to extend this method to the galaxies, we model their halo-occupation number $\langle N_g|M\rangle$ that gives the mean number of galaxies contained within a single dark-matter halo of mass M. Uncountable studies have shown that, for galaxies selected by luminosity in a broadband optical filter (or by stellar mass), $\langle N_g|M\rangle$ can be well approximated by the sum of a step function (describing central galaxies and ranging between 0 and 1) and a power law (describing satellite galaxies). However, when galaxies are selected by the intensity of an emission line (or by star-formation rate), $\langle N_g|M\rangle$ is better described by a uni-modal function that always assumes values smaller than one (for the central galaxies) plus a power law (for the satellites). The latter parametrization has been used by Geach et al. (2012) to model the observed clustering of H α emitters at $z \sim 2.2$ and by Gonzalez-Perez et al. (2018) to describe the population of [O II] emitters in a semi-analytic model of galaxy formation. We approximate their results by using a simple expression containing a free parameter (M_0) that determines the typical halo mass and a second one ($\mathcal{N}_{\rm HO} \leq 0.95$) that fixes the overall normalization:

$$\langle N_g|M\rangle = \mathcal{N}_{\rm HO}\left(\langle N_c|M\rangle + \langle N_s|M\rangle\right) \tag{44}$$

with

$$\langle N_c|M\rangle = \exp\left\{-10\left[\log_{10}\left(\frac{M}{M_0}\right)\right]^2\right\} + 0.05\,\Theta\left(\frac{M}{M_0}\right), \tag{45}$$

$$\langle N_s|M\rangle = 0.003\,\frac{M}{M_0}\,\Theta\left(\frac{M}{M_0}\right), \tag{46}$$

and

$$\Theta\left(\frac{M}{M_0}\right) = 1 + {\rm erf}\left[2\log_{10}\left(\frac{M}{M_0}\right)\right]. \tag{47}$$

The first term on the right-hand side of equation (44) describes the halo occupation number of central galaxies while the second one refers to satellite galaxies. Here, M_0 denotes the halo mass at which the mean number of central galaxies reaches its maximum. Given the halo mass function $n(M)$ in each redshift bin (Sheth, Mo & Tormen 2001), we determine M_0 by requiring that the effective linear bias of the *Euclid* galaxies

$$b_{\rm eff} = \frac{\int b_1(M)\,n(M)\,\langle N_g|M\rangle\,{\rm d}M}{\int n(M)\,\langle N_g|M\rangle\,{\rm d}M} \tag{48}$$

coincides with the fit given in Pozzetti et al. (2016). Using the resulting M_0, we then determine the effective value of b_2 by averaging the quadratic halo bias with weights given by the mass function and the halo occupation number as in equation (48). We have checked the stability of our results with respect to the parametrization of the halo mass function (Bhattacharya et al. 2011 and references therein). Note that, since the halo tidal bias depends linearly on b_1, we can obtain b_{s^2} for the galaxies directly from their linear bias. The complete set of the bias coefficients we obtain is listed in Table 1. It is worth stressing that the values of b_2 are always slightly less negative than (but very close to) those that would be obtained from b_1 by straightforwardly applying the relation between the bias parameters that holds for dark-matter haloes. This shows that the details of the halo-occupation model are not very important for determining b_2 and strengthen our confidence in the approximate methods we have used. For the sake of completeness, in Fig. 3, we plot the halo-occupation number of the *Euclid* galaxies at different redshifts. The normalization constant $\mathcal{N}_{\rm HO}$(unnecessary to determine the bias coefficients) is obtained by requiring that $n_g = \int n(M)\,\langle N_g|M\rangle\,{\rm d}M$ (see Table 1).

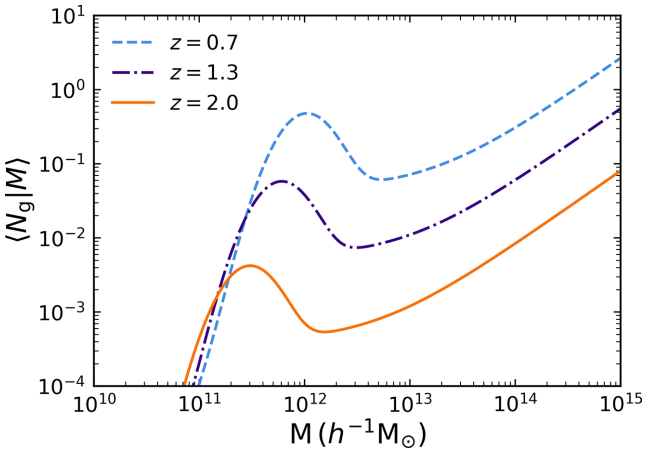

Figure 3. Halo-occupation number of the *Euclid* galaxies at different redshifts.

The last parameter we need to fix in order to build a fiducial model for the power spectrum and the bispectrum of *Euclid* galaxies is the rescaled pairwise velocity dispersion, $\sigma_{\rm p}$. As we briefly mentioned above, N-body simulations suggest that, at the redshifts of interest here, $\sigma_{\rm p}$ can be well approximated by linear-theory predictions (Hashimoto et al. 2017). Therefore, neglecting velocity bias, we write $\sigma_{\rm p}^2 = 2\,\sigma_v^2$ (where $a\,H\,\sigma_v$ denotes the 1-dimensional velocity dispersion for the dark matter) with

$$\sigma_v^2 = \frac{f^2}{3}\int_0^\infty \frac{P_{\rm L}(k)}{k^2}\,\frac{{\rm d}^3k}{(2\pi)^3} = \frac{f^2}{6\pi^2}\int_0^\infty P_{\rm L}(k)\,{\rm d}k\,. \tag{49}$$

Our results are summarized in Table 1.

3.4 Cosmological models

Within the CDM scenario with Gaussian initial conditions, we consider three classes of cosmological models characterized by different parametrizations for the equation-of-state parameter of dark energy, w.

We first examine plain vanilla CDM models with a cosmological constant, where $w = -1$ (ΛCDM). They are controlled by five parameters. The present-day values of the density parameters for dark matter, $\Omega_{\rm cdm}$, and baryons, $\Omega_{\rm b}$, as well as the Hubble constant, h, fully determine the background. At the same time, we assume a power-law form for the power spectrum of primordial (scalar, adiabatic) curvature perturbations

$$\mathcal{P}_{\mathcal{R}}(k) = A\left(\frac{k}{k_*}\right)^{n_{\rm s}-1}, \tag{50}$$

which is then completely determined by the spectral index $n_{\rm s}$ and the amplitude A at the pivot scale $k_* = 0.05\ {\rm Mpc}^{-1}$.

The simplest extension to ΛCDM we consider is a phenomenological model in which w stays constant with time but can assume

values different from -1. We refer to this case, where w is treated as a sixth cosmological parameter, as wCDM.

The next level of complexity is to use two parameters to describe a time-varying equation of state (see e.g. Sahni & Starobinsky 2006, for a review). We adopt the popular choice of assuming that w evolves linearly with a and write

$$w = w_0 + w_a\,(1-a) \tag{51}$$

(Chevallier & Polarski 2001; Linder 2003). Here, w_0 gives the present-day value of the equation-of-state parameter, while w_a describes its current rate of change. Although, these phenomenological parameters provide a useful tool to detect deviations from a cosmological constant from experiments, it is not straightforward to map them on to physical dark-energy models (e.g. Scherrer 2015). Note that equation (51) describes a monotonic (and rather gentle) evolution from the primordial value of $w_0 + w_a$ to w_0.

In all cases, as a fiducial model we use the ΛCDM solution with the best-fitting parameters for the 'TT+lowP + lensing' *Planck* 2015 results (Planck Collaboration XIII 2016): namely, $\Omega_{\rm cdm} = 0.2596$, $\Omega_{\rm b} = 0.0484$, $h = 0.6781$, $n_s = 0.9677$, $A = 2.139 \times 10^{-9}$, and $w = -1$. Linear transfer functions for the matter perturbations are computed using the CAMB code (https://camb.info, Lewis, Challinor & Lasenby 2000; Howlett et al. 2012).

3.5 Method

For each redshift interval, we build a data vector that combines the (shot-noise corrected) expectation values for the galaxy power spectrum and the bispectrum in the selected configuration bins. Schematically, we write $\mathbf{D} = (P, B)$ and we compute the Fisher information matrix

$$F_{\alpha\beta} = \frac{\partial \mathbf{D}}{\partial p_\alpha} \cdot \mathbf{C}^{-1} \cdot \frac{\partial \mathbf{D}^T}{\partial p_\beta}\,, \tag{52}$$

where p_α and p_β indicate two of the model parameters and $\mathbf{C}$ is the block covariance matrix

$$\mathbf{C} = \begin{pmatrix} \mathbf{C}_{\rm PP} & \mathbf{C}_{\rm PB} \\ \mathbf{C}_{\rm BP} & \mathbf{C}_{\rm BB} \end{pmatrix} \tag{53}$$

that can be conveniently inverted using

$$\mathbf{C}^{-1} = \begin{pmatrix} \mathbf{C}_{\rm A} & -\mathbf{C}_{\rm A}\mathbf{C}_{\rm PB}\mathbf{C}_{\rm BB}^{-1} \\ -\mathbf{C}_{\rm BB}^{-1}\mathbf{C}_{\rm BP}\mathbf{C}_{\rm A} & \mathbf{C}_{\rm BB}^{-1} + \mathbf{C}_{\rm BB}^{-1}\mathbf{C}_{\rm BP}\mathbf{C}_{\rm A}\mathbf{C}_{\rm PB}\mathbf{C}_{\rm BB}^{-1} \end{pmatrix}\,, \tag{54}$$

with $\mathbf{C}_{\rm A} = (\mathbf{C}_{\rm PP} - \mathbf{C}_{\rm PB}\mathbf{C}_{\rm BB}^{-1}\mathbf{C}_{\rm BP})^{-1}$. We then sum the partial Fisher information matrices obtained for the different redshift intervals and invert the resulting matrix to make a forecast for the covariance matrix of the model parameters.

As a reference case, we consider wavevectors with $k < k_{\rm max}$, where $k_{\rm max} = 0.15\,h$ Mpc^{-1}. This is for three reasons. First, with the current state of the art, it is challenging to model non-linearities in P and B for much larger wavenumbers with an accuracy that allows applications to precision cosmology. Lazanu et al. (2016) have recently tested various models for the real-space bispectrum of matter perturbations against N-body simulations. To the lowest non-vanishing order (tree level), SPT statistically matches the numerical results to better than 5 per cent up to $k_{\rm max} = 0.17\,h$ Mpc^{-1} for $z = 1$ and $k_{\rm max} = 0.20\,h$ Mpc^{-1} for $z = 2$. Extending the calculation to next-to-leading order (i.e. adding one-loop corrections) considerably broadens the range of validity of the theory at $z \sim 2$. Substantially larger values for $k_{\rm max}$ at all redshifts (by up to a factor of two, see table II in Lazanu et al. 2016) can also be obtained by either reorganizing the perturbative expansion (e.g. Matsubara 2008; Crocce, Scoccimarro & Bernardeau 2012) or by adopting an effective-field-theory approach in which the influence of non-perturbative small-scale physics on to the large-scale perturbations is described with modified fluid equations whose extra parameters are calibrated against numerical simulations (e.g. Baumann et al. 2012; Carrasco, Hertzberg & Senatore 2012; Angulo et al. 2014; Baldauf et al. 2015). However, accounting for galaxy biasing, RSD and discreteness effects provide additional challenges for the perturbative models and reduces their range of validity. Secondly, the numerical inversion of $\mathbf{C}$ becomes more and more demanding with increasing $k_{\rm max}$. In fact, since we use a minimal bin size of $\Delta k = k_{\rm f}$, we end up dealing with very high-dimensional matrices mainly due to the large number of possible triangle configurations for the bispectrum. Our default choice is to use 8 bins (i.e. $N_{\rm p} = 4$ and $N_{\rm a} = 2$) for the triangle orientations with respect to the line of sight. In this case, we use between approximately 31 200 and 65 500 bispectrum bins. Although the outcome of our study does not depend on the adopted angular coordinate system, we only show results obtained by taking bins in $\cos\tilde{\theta}$ and $\tilde{\phi}$. A third motivation for limiting our study to $k_{\rm max} = 0.15\,h$ Mpc^{-1} is that non-linear effects strongly enhance the non-Gaussian contributions for all the sub-matrices that form $\mathbf{C}$ (e.g. Chan & Blot 2017). In consequence, the information content of P and B strongly deviates from simplistic expectations based on counting Fourier modes. For instance, when one analyses the power spectrum, these effects lead to the so-called translinear information plateau (Rimes & Hamilton 2005; Neyrinck & Szapudi 2007; Takahashi et al. 2009). Basically, with increasing $k_{\rm max}$, the cumulative information about a cosmological parameter grows until it saturates (for $k_{\rm max} \gtrsim 0.2\,h$ Mpc^{-1}). Only by analysing much smaller (non-perturbative) scales ($k_{\rm max} \gg 1\,h$ Mpc^{-1}) can one retrieve useful information again. Although there are indications that the cumulative information stored in the bispectrum might saturate at smaller scales than for the power spectrum, it is also evident that, in the mildly non-linear regime, it increases at a much smaller rate than in the Gaussian approximation (Kayo, Takada & Jain 2013; Chan & Blot 2017). These considerations, together with the fact that the hierarchy of correlation functions (and their Fourier transforms) should be a rather inefficient tool to retrieve information from perturbations on fully non-linear scales (Carron 2012; Carron & Neyrinck 2012), have motivated alternative approaches for retrieving the information based on non-linear transforms and Gaussianization procedures (e.g. Carron & Szapudi 2014 and references therein).

In Table 2, we summarize the cosmological and nuisance parameters used in our main investigation. As detailed in Section 3.4, the cosmology is specified by fixing 5–7 variables depending on the adopted parametrization of the dark-energy equation of state. In parallel, for each redshift bin, we consider three bias parameters and the pairwise velocity dispersion, for a total of 56 nuisance parameters that characterize the galaxy population under study. In Section 5, we will discuss some modifications to this set-up and their implications.

3.6 Priors

Bayesian statistics requires adopting a prior probability distribution for the model parameters. In this regard, we perform our analysis in two steps. First, we study the constraining power on cosmology of a *Euclid*-like survey by itself. In this case, we use directly the Fisher matrix to produce our forecasts. This procedure only uses information from the likelihood function and corresponds to adopting very diffuse priors on all the parameters. Subsequently, we

Table 2. Summary of the cosmological models considered in this paper. Here, $N_{\rm par}$ indicates the total number of free parameters in the fit, while the last column gives the name of the Monte Carlo generated Markov chains for the *Planck* data we use to generate the prior.

Model	$N_{\rm par}$	Cosmology	Bias 14 z-bins	Nuisance 14 z-bins	*Planck* sample
ΛCDM	61	$\Omega_{\rm cdm}$, $\Omega_{\rm b}$, h, n_s, A	$b_1(z)$, $b_2(z)$, $b_{s^2}(z)$	$\sigma_{\rm p}(z)$	base-plikHM-TTTEEE-lowTEB
wCDM	62	$\Omega_{\rm cdm}$, $\Omega_{\rm b}$, h, n_s, A, w	$b_1(z)$, $b_2(z)$, $b_{s^2}(z)$	$\sigma_{\rm p}(z)$	w-base-plikHM-TTTEEE-lowTEB
w_0w_aCDM	63	$\Omega_{\rm cdm}$, $\Omega_{\rm b}$, h, n_s, A, w_0, w_a	$b_1(z)$, $b_2(z)$, $b_{s^2}(z)$	$\sigma_{\rm p}(z)$	base-w-wa-plikHM-TT-lowTEB-BAO

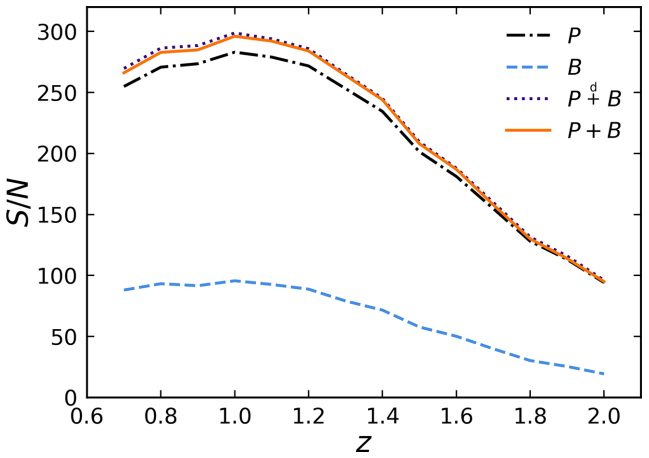

Figure 4. S/N for measurements of the galaxy power spectrum and the bispectrum in a *Euclid*-like survey as a function of redshift. We show results for the redshift-space power spectrum (dot–dashed), the redshift-space bispectrum (dashed), and their combination (solid). For comparison, we also display the S/N computed by neglecting the cross-covariance between P and B (dotted).

combine the results of this first exercise with the constraints coming from the study of cosmic-microwave-background anisotropies performed by the *Planck* mission. To do this, we proceed as follows. For each of the cosmological models introduced in Section 3.4, we download a Markov chain that samples the posterior distribution from the *Planck* web-page[3] and compute the corresponding covariance matrix for the subset of cosmological parameters considered here. We then invert the covariance matrix and sum the result to the *Euclid*-like Fisher matrix. In practice, we treat the *Planck* results as Gaussian priors for our study of galaxy clustering. The exact names of the files we use are reported in Table 2. Note that, for the w_0w_aCDM models, we use a combination of current CMB and galaxy-clustering data.

4 RESULTS

4.1 Signal-to-noise ratio

In Fig. 4, we quantify the statistical significance with which the redshift-space power spectrum and bispectrum of *Euclid* galaxies will be measured. We plot the S/N

$$\left(\frac{S}{N}\right)^2 = \mathbf{D}\cdot\mathbf{C}^{-1}\cdot\mathbf{D}^T\,, \tag{55}$$

as a function of redshift (solid). We also show individual results for P (dot–dashed) and for B (dashed) as well as for their combination when the cross-covariance $\mathbf{C}_{\rm PB}$ is assumed to vanish (dotted). Thanks to the huge volume covered by the *Euclid*-like survey, both the power spectrum and the bispectrum are clearly distinguishable from noise with high confidence (note that this is not true for the single triangular configurations of the bispectrum whose measurement, given our narrow bins in k, is almost always dominated by noise). The global S/N, however, rapidly drops for $z > 1.2$ mainly due to the decreasing galaxy number density. In spite of the very large number of triangular configurations, we consider that the S/N for B is always a factor of 2.5–3 times smaller than for P. Finally, we note that neglecting the cross-covariance between P and B, as in some previous studies (e.g. Karagiannis et al. 2018), only slightly overestimates the total S/N at the lowest redshifts (see also Song et al. 2015). This is a consequence of the fact that we only consider quasi-linear scales where P and B are weakly correlated. The differences become more marked if the analysis is extended to smaller scales (Byun et al. 2017; Chan & Blot 2017).

4.2 Cosmological parameters

In Figs 5–7, we show the results of our forecasts for the ΛCDM, wCDM, and w_0w_aCDM models, respectively. Shown are the joint 68.3 per cent credible regions for all possible pairs of cosmological parameters obtained after marginalizing over all the remaining model parameters. The bottom-left area of the figures is tailored to display the likelihood contours obtained from a *Euclid*-like survey. Dot–dashed, dashed, and solid lines show the constraints coming from the galaxy power spectrum, the bispectrum, and their combination, respectively. In each panel, we report the ratio between the areas enclosed within the dot–dashed and the solid curves. These numbers show that the benefit of combining two- and three-point statistics becomes more marked for the models that include a larger number of free parameters as there are more degeneracies to break. On the other hand, the narrow-shaded regions highlight the credible regions obtained by also considering the *Planck* priors introduced in Section 3.6. The top-right areas of the figures zoom in to display the combined results more clearly.

The corresponding marginalized errors for each single variable are reported in Table 3. In general, the bispectrum provides similar, but slightly worse, constraints than the power spectrum. Also, the orientation of the likelihood contours is very similar between the two probes. Therefore, the combination of these two- and three-point statistics leads to a non-negligible but moderate gain in the determination of the cosmological parameters.

Adding the *Planck* prior breaks degeneracies in the models by imposing strong constraints on $n_{\rm s}$, A, as well as on various combinations of $\Omega_{\rm b}$, h. In consequence, the parameters that describe the dark-energy equation of state are determined much more precisely. Once combined with *Planck*, the galaxy power spectrum and the bispectrum give very similar constraints on the cosmological parameters. In this case, combining two- and three-point statistics

[3] https://wiki.cosmos.esa.int/planckpla2015/index.php/ Cosmological_Parameters

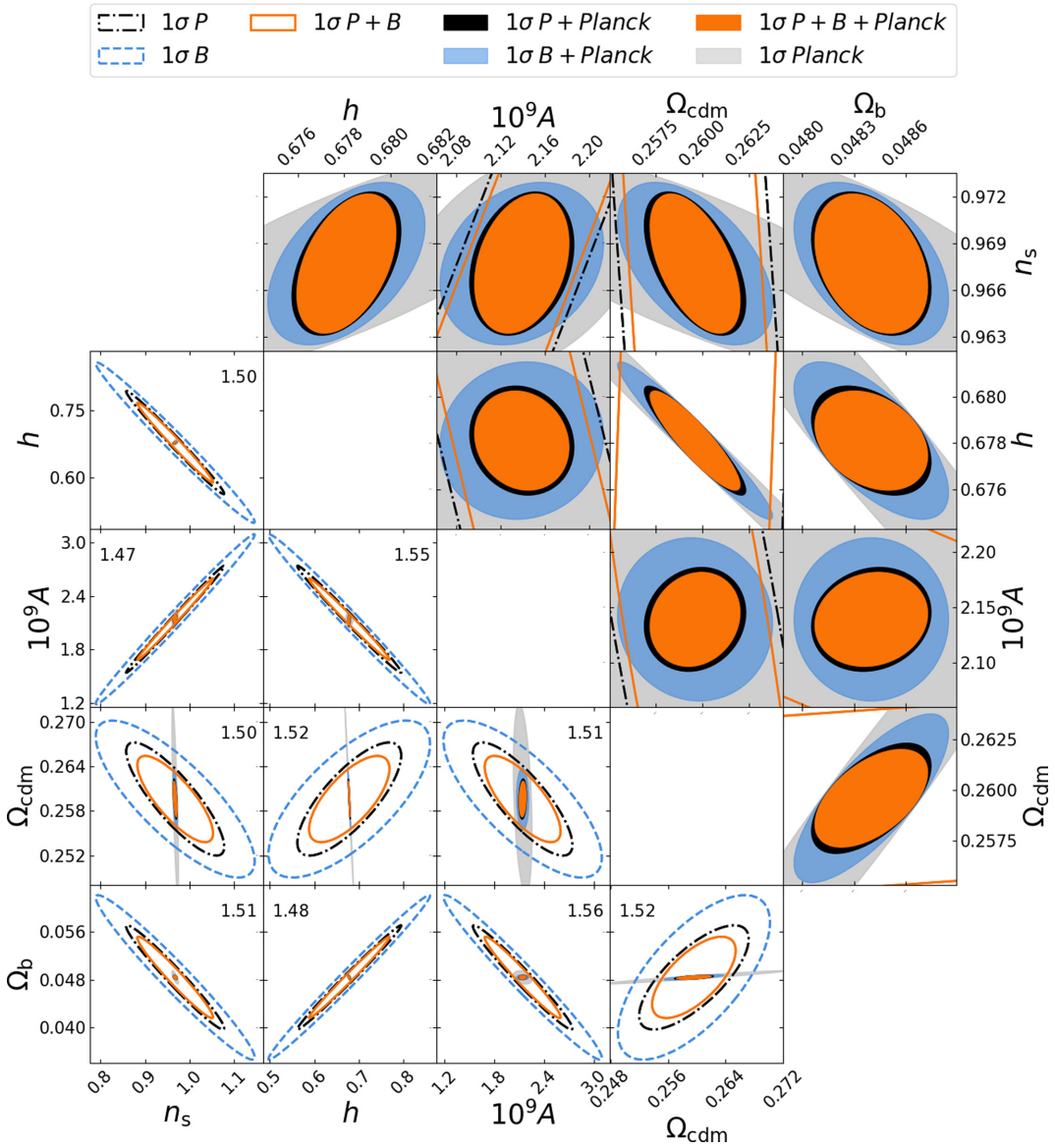

Figure 5. Joint 68.3 per cent credible regions for all pairs of cosmological parameters of the ΛCDM model. Different linestyles indicate the forecast for a *Euclid*-like survey based on different observables: namely, the power spectrum (dot–dashed), the bispectrum (dashed), and their combination (solid). The numbers indicate the ratio between the areas enclosed within the dot–dashed and the solid lines. The shaded areas highlight the credible regions obtained by also considering the *Planck* priors introduced in Section 3.6. The colour coding is indicated by the top labels. The panels below the diagonal offer a panoramic view while those above the diagonal zoom in for a close up of the central regions.

provides only minimal advantages for the cosmology sector but yields a precise measurement of galaxy bias (see Section 4.3).

Table 3 also shows that the forecast obtained by neglecting the cross-covariance between P and B is only slightly optimistic with respect to the full analysis. This result validates previous studies that do not consider $\mathbf{C}_{\rm BP}$ (provided that they focus on sufficiently large scales). Note that the numerically challenging inversion of the covariance matrix in equation (52) becomes trivial when $\mathbf{C}_{\rm BP} = 0$.

4.3 Galaxy bias

Being able to accurately measure non-linear galaxy bias is considered one of the classic advantages of bispectrum studies. In Fig. 8, we present forecasts for the uncertainty with which an *Euclid*-like survey can determine the bias parameters in a ΛCDM model (results are similar for the other cases considered in this paper). The bispectrum provides tight constraints on the bias coefficients at low redshift, but it does not contain enough information to uniquely determine them at higher redshifts where estimates of b_1 and b_2 (and, to a lesser degree, b_1 and b_{s^2}) are degenerate. Simultaneously, fitting the power spectrum and the bispectrum strongly improves the situation. In fact, the power spectrum more tightly constraints b_1 (see also Fig. 9) and this is enough to break the degeneracies with b_2 and b_{s^2}. Combining the two probes, leads to even smaller b_1 errors, especially for the w_0w_aCDM model (rightmost panel in Fig. 9). It is worth stressing that, in a power-spectrum study, the error

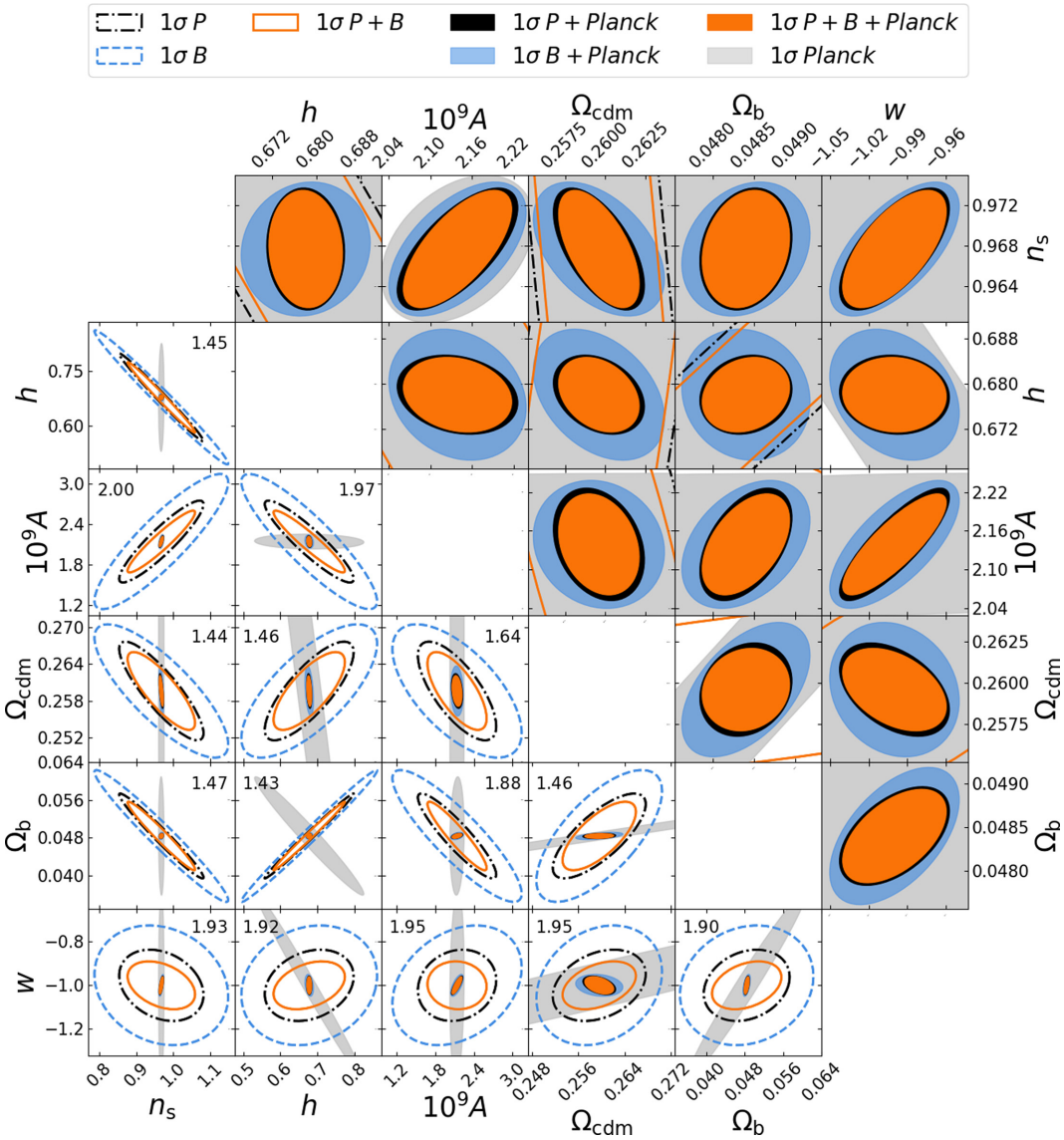

Figure 6. As in Fig. 5 but for the wCDM model.

on b_1 correlates with that on most cosmological parameters while cosmology-bias cross-correlations are weaker for the bispectrum.

Fig. 8 shows that the combination of power spectrum and bispectrum should provide rather tight constraints in the (b_1, b_2, b_{s^2}) space that could be used to derive the halo occupation properties of the galaxies. In fact, empirically measuring deterministic relations between b_1 and b_2 as well as between b_1 and b_{s^2} would shed light on the nature of the biasing process. For instance, measuring a negative b_{s^2} at all redshifts in accordance with equation (43) would provide evidence in favour of a local biasing process in Lagrangian space.

4.4 Figure of merit for dark-energy constraints

Since the report of the dark-energy task force (DETF; Albrecht et al. 2006), it is customary to compare cosmological probes in terms of a conveniently defined figure of merit (FoM), i.e. a single number summarizing the strength of the constraints that can be set on to the model parameters that describe dynamic dark energy. For the w_0w_aCDM model, we adopt the definition (Wang 2008; Mortonson, Huterer & Hu 2010)

$$\mathrm{FoM} = \frac{1}{\sqrt{\det \mathrm{Cov}(w_0,\, w_a)}}\,, \tag{56}$$

where $\mathrm{Cov}(w_0,\, w_a)$ denotes the 2×2 covariance matrix for the errors on w_0 and w_a (note that our definition is a factor of 6.17π larger than the DETF FoM that is defined as the reciprocal of the area in the w_0-w_a plane that encloses the 95 per cent credible region). Our results are reported in the last row of Table 3. We find that the galaxy power spectrum in a *Euclid*-like survey gives an FoM that is more than two times larger than for the bispectrum. However, combining two- and three-point statistics improves the FoM by a factor of 2.6 with respect to considering the power spectrum only.[4] This promising result is, however, weakened by considering the

[4]The corresponding factors for other combinations of cosmological parameters can be directly read in the bottom left-hand panels of Figs 5–7.

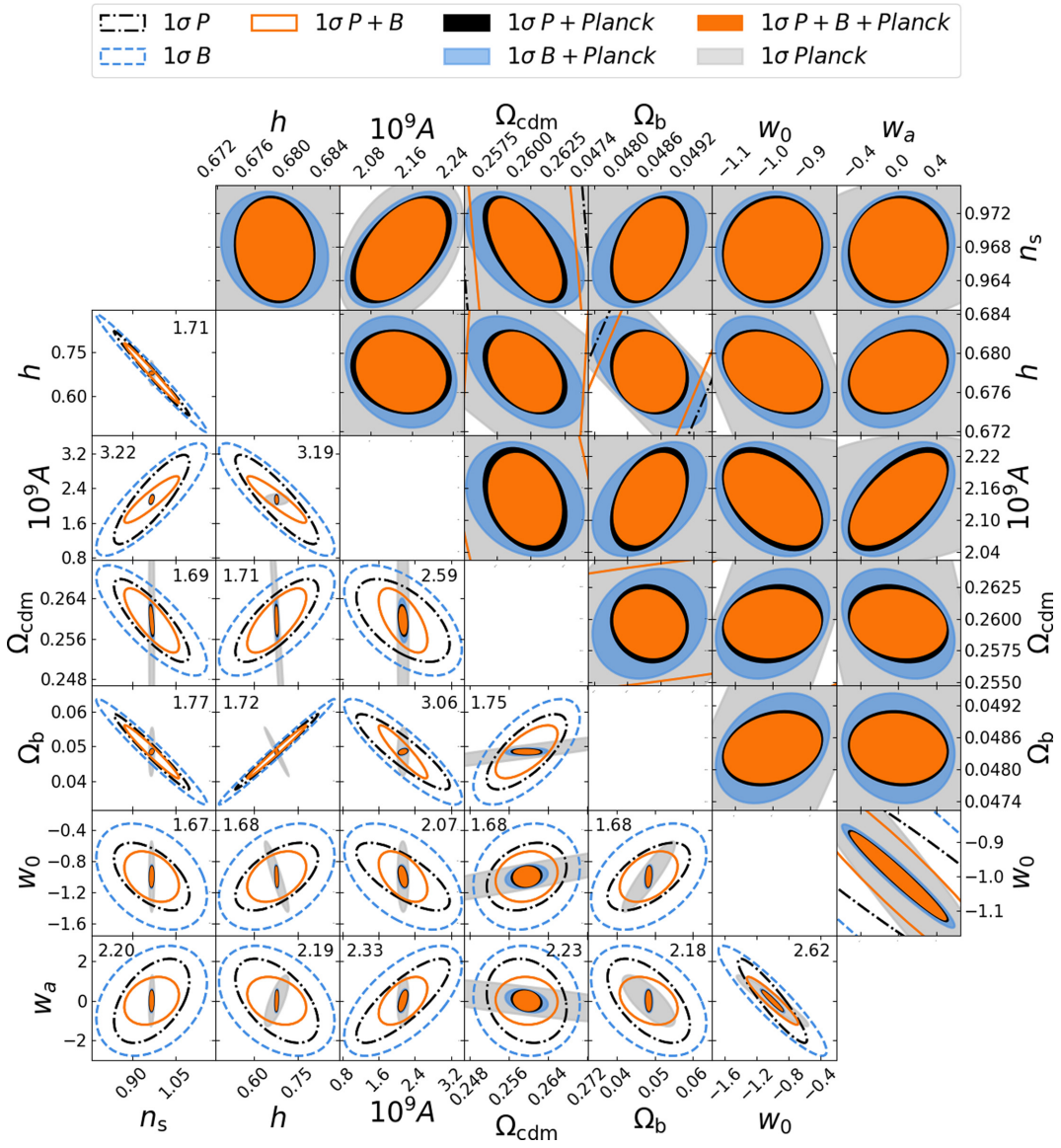

Figure 7. As in Fig. 5 but for the w_0w_aCDM model.

current CMB + clustering constraints as a prior. In this case, adding the bispectrum only improves the FoM by 11 per cent. The reason for this behaviour is as follows. The improvement for the *Euclid* data mainly derives from partially breaking the degeneracy between b_1 and the amplitude of P and B for all redshift bins. As we have shown in the previous Section, combining P and B allows a much better determination of the linear bias parameters at all redshifts (the marginalized errors shrink by a factor between 2 and 3). These 14 parameters are degenerate with the amplitudes of the clustering signals that depend on both A and the linear growth factors (thus on w_0 and w_a).[5] Once the *Planck*'s data are taken into consideration, A is extremely well determined and the constraints on b_1, w_0, and w_a do not improve significantly by adding the galaxy bispectrum to the power spectrum.

[5]We have checked that, if the linear bias coefficients are kept fixed at their fiducial value, the FoM for the dark-energy parameters only improves by a factor of 1.25 when P and B are combined.

5 DISCUSSION

In this section, we study how modifications to our standard setup influence the forecast results. For simplicity, we only consider the ΛCDM model and focus on the redshift bin centred at $z = 1$.

5.1 Dependence on the bin width Δk

So far, we have presented results obtained using narrow wavenumber bins with $\Delta k = k_f$. This choice is motivated by the trade-off between minimizing information loss and taking into account the effect of the window function of the survey. However, it is difficult to imagine that such narrow bins will be ever used in actual observational studies. This is mainly because the large dimensionality of

Table 3. Expected marginalized 1σ errors (i.e. half of the 68.3 per cent credible-interval size) for the cosmological parameters in the ΛCDM, wCDM, and w_0w_aCDM models obtained considering a *Euclid*-like survey (left) and its combination with *Planck* priors (right). The different columns display results obtained from the galaxy power spectrum, P, the bispectrum, B, and their combination, $P+B$. We also show forecasts computed by neglecting the cross-covariance $\mathbf{C}_{\rm BP}$ that we indicate with the symbol $P \overset{\rm d}{+} B$. Note that, to ease the presentation of the results, the parameters have been rescaled by a multiplicative factor as indicated in the leftmost column of each sector. The bottom row gives the figure of merit for the dark-energy parameters w_0 and w_a.

	Euclid-like alone					*Euclid*-like with *Planck* prior			
	P	B	$P \overset{\rm d}{+} B$	$P+B$		P	B	$P \overset{\rm d}{+} B$	$P+B$
				ΛCDM					
$10\,n_{\rm s}$	0.72	1.17	0.53	0.56	$10^3\,n_{\rm s}$	3.02	3.43	2.91	2.93
$10\,h$	0.76	1.19	0.56	0.59	$10^3\,h$	1.55	2.24	1.38	1.41
$10^{10}A$	3.95	6.28	2.87	3.01	$10^{11}A$	3.09	4.86	2.60	2.80
$10^3\,\Omega_{\rm cdm}$	5.01	6.96	3.56	3.82	$10^3\,\Omega_{\rm cdm}$	1.79	2.73	1.54	1.58
$10^3\,\Omega_{\rm b}$	5.71	9.02	4.26	4.46	$10^4\,\Omega_{\rm b}$	2.27	2.94	2.12	2.14
				wCDM					
$10\,n_{\rm s}$	0.75	1.19	0.56	0.60	$10^3\,n_{\rm s}$	3.96	4.35	3.78	3.81
$10\,h$	0.79	1.21	0.59	0.63	$10^3\,h$	4.61	7.64	4.27	4.35
$10^{10}A$	3.99	6.58	2.87	3.01	$10^{11}A$	5.73	6.52	5.08	5.14
$10^3\,\Omega_{\rm cdm}$	5.28	7.14	3.83	4.17	$10^3\,\Omega_{\rm cdm}$	1.86	2.68	1.61	1.64
$10^3\,\Omega_{\rm b}$	5.87	9.13	4.45	4.74	$10^4\,\Omega_{\rm b}$	3.69	5.13	3.45	3.49
$10\,w$	1.07	1.80	0.71	0.72	$10^2\,w$	2.80	3.30	2.61	2.64
				w_0w_aCDM					
$10\,n_{\rm s}$	0.86	1.26	0.58	0.62	$10^3\,n_{\rm s}$	4.13	4.52	3.92	3.96
$10\,h$	0.93	1.30	0.62	0.66	$10^3\,h$	2.78	3.74	2.65	2.67
$10^{10}A$	6.78	8.55	3.48	3.54	$10^{11}A$	6.32	7.07	5.62	5.67
$10^3\,\Omega_{\rm cdm}$	5.37	7.16	3.83	4.17	$10^3\,\Omega_{\rm cdm}$	2.00	2.85	1.71	1.77
$10^3\,\Omega_{\rm b}$	7.12	9.99	4.75	5.02	$10^4\,\Omega_{\rm b}$	4.59	6.81	4.21	4.26
$10\,w_0$	2.85	4.47	2.00	2.13	$10^2\,w_0$	8.61	9.88	8.28	8.38
w_a	1.40	1.83	0.78	0.79	$10\,w_a$	3.40	3.88	3.26	3.29
FoM(w_0w_a)	6.66	3.03	18.10	17.43	FoM(w_0w_a)	147.06	93.32	166.71	162.49

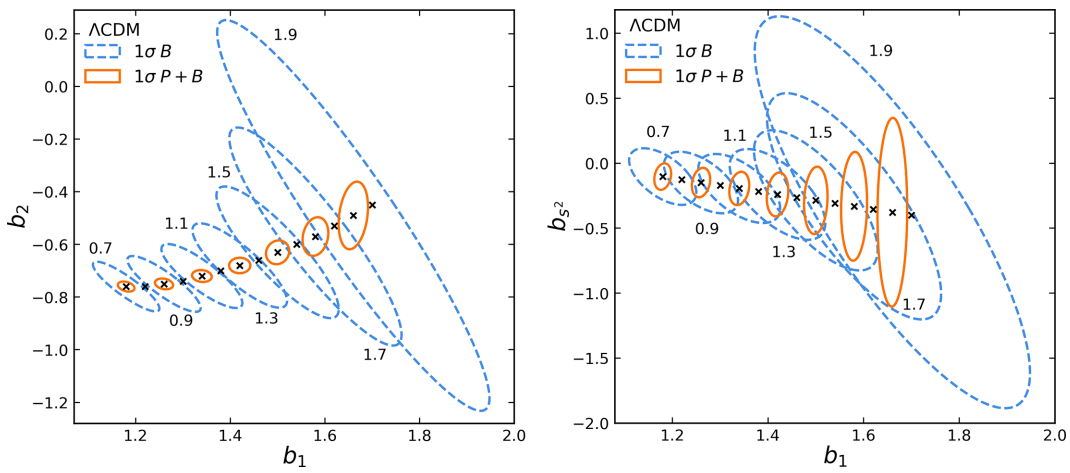

Figure 8. Joint 68.3 per cent credible regions for pairs of bias parameters determined using the bispectrum (dashed) and the combination between the power spectrum and the bispectrum (solid) for a *Euclid*-like survey. To improve readability, we mark with crosses the fiducial values for all redshift bins but we show the credible regions only for alternate bins. The mean redshift for the sample increases from left to right. The numerical labels indicate the central value of each redshift bin and are located in proximity of the corresponding contours to help identify them.

the data makes the estimation of covariance matrices prohibitive, at least when it is done using a large number of mock galaxy catalogues. Here, we quantify the influence of the bin size Δk on the forecast results. As a measure of information content, we generalize the definition of FoM given in equation (56) and write

$$\mathrm{FoM} = \frac{1}{\sqrt{\det \mathrm{Cov}(p_1,\ldots,p_n)}}\,, \tag{57}$$

where $(p_1,\ldots,p_n)$ denotes the set of model parameters that belong to a given sector (e.g. 'cosmology', 'bias', etc.). Note that the quantity $\mathrm{FoM}^{1/n}$ gives an effective error estimate for a single parameter. In Fig. 10, we illustrate how the forecast constraints from the analysis of the power spectrum and the bispectrum degrade as the size of Δk increases. Shown is the ratio $\mathrm{FoM}^{1/n}(\Delta k)/\mathrm{FoM}^{1/n}(\Delta k = k_{\rm f})$ that provides an indication of the mean information loss per model parameter and allows us to easily compare results obtained for

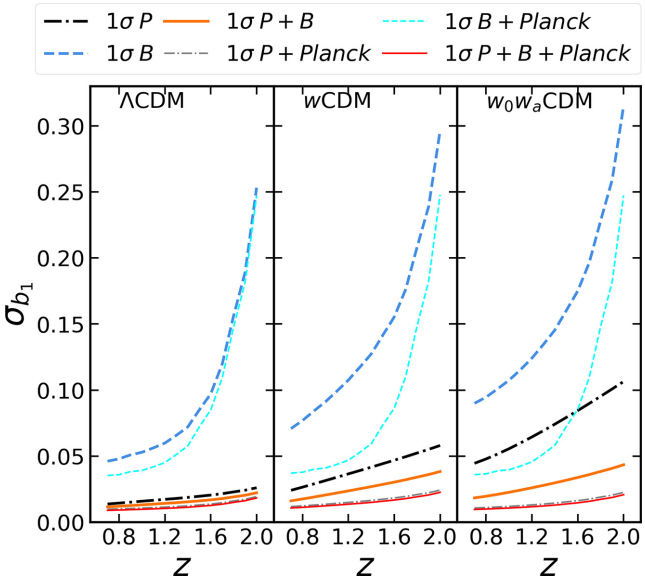

Figure 9. Forecast 1σ errors for the linear bias parameter as a function of redshift. Shown are the results for a *Euclid*-like survey (with and without *Planck* priors) based on the galaxy power spectrum (dot–dashed), the bispectrum (dashed), and their combination (solid). Line style and thickness are indicated by the top labels.

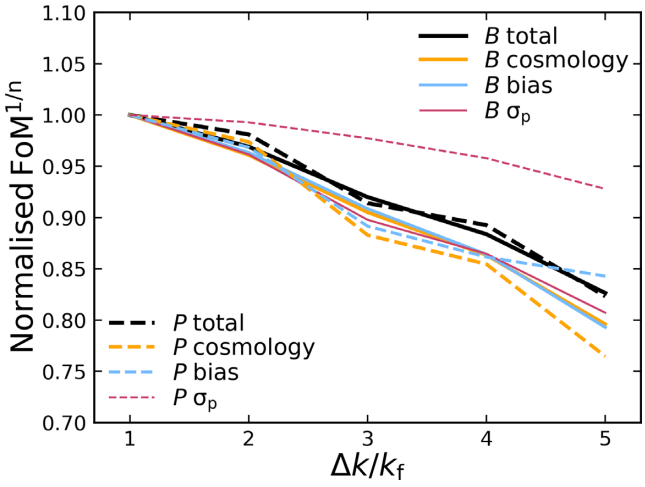

Figure 10. Typical information loss per model parameter as a function of the bin size Δk. Shown is the function $\mathrm{FoM}^{1/n}(\Delta k)$ normalized to one at $\Delta k = k_\mathrm{f}$ (the value we used in Section 4). Results for the power spectrum and the bispectrum measured from a *Euclid*-like survey at $0.95 < z < 1.05$ are shown with dashed and solid lines, respectively. Model parameters are grouped in different sectors as indicated by the labels. The figure refers to the ΛCDM model.

different sectors. In all cases, the deterioration of the constraints with increasing Δk is noticeable. For instance, using $\Delta k = 5k_\mathrm{f}$ typically leads to error bars on the model parameters that are 20 per cent larger than in our reference case. Note that the recent analysis of the bispectrum monopole from the BOSS DR12 CMASS sample (Gil-Marín et al. 2017) adopts $\Delta k = 6k_\mathrm{f}$ due to the limited number of mock catalogues available to estimate the covariance matrix. It is only by compressing the data vector with the Karhunen–Loève transform that Gualdi et al. (2018b) could employ thinner k-bins down to $\Delta k = 2k_\mathrm{f}$.

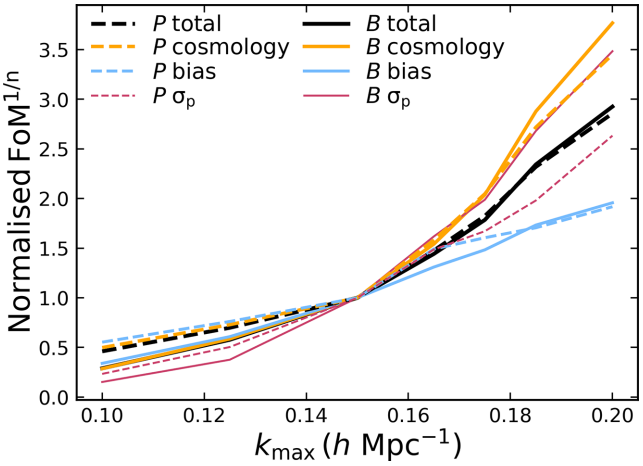

Figure 11. As in Fig. 10 but as a function of k_max.

5.2 Dependence on k_max

The results presented in Section 4 have been obtained considering all Fourier modes with $k < k_\mathrm{max} = 0.15\,h$ Mpc^{-1}. This choice was dictated primarily by theoretical limitations. In fact, it is challenging to develop models for the galaxy bispectrum in redshift space that are sufficiently accurate on smaller scales. However, it is difficult to draw a precise line that marks where models lose their predictive power. For this reason, here we explore how the Fisher-matrix forecast depends on the choice of k_max. An alternative approach would be to include 'theoretical errors' in the likelihood and extend the analysis to large wavenumbers (Baldauf et al. 2016). Though, this would force us to always deal with impractically large covariance matrices and, also, assumptions would have to be made in order to estimate the size of the theoretical errors for the bispectrum in redshift space. For these reasons, we prefer to use the more traditional method of varying k_max. Our results are presented in Fig. 11. For the cosmology sector, the quantity $\mathrm{FoM}^{1/n}$ scales as k_max^α with $\alpha \simeq 2.7$ for the power spectrum and $\alpha \simeq 3.6$ for the bispectrum. If these scaling properties can be extrapolated beyond $0.2\,h$ Mpc^{-1}, our results imply that the bispectrum will achieve the same constraining power as the power spectrum for $k_\mathrm{max} \sim 0.43\,h$ Mpc^{-1}.

5.3 Binning of triangle orientations

In Fig. 12, we investigate how the quantity $\mathrm{FoM}^{1/n}$ depends on the number of bins used to describe the orientation of the triangular configurations for the bispectrum with respect to the line of sight. For simplicity, we only show results for the complete fit including all cosmological and nuisance parameters (that we labelled 'total' in Figs 10 and 11), as the individual plots for the different sectors all appear very similar. The first important thing to mention is that just considering the monopole of the bispectrum in redshift space (i.e. $N_{\tilde{\phi}} = N_{\tilde{\mu}_1} = 1$) leads to a non-negligible loss of information. In this case, individual parameter constraints degrade, on average, by ∼30 per cent with respect to our reference case ($N_{\tilde{\phi}} = 2$, $N_{\tilde{\mu}_1} = 4$). Taking into account the lowest-order non-vanishing multipoles with $m = 0$ (i.e. setting $N_{\tilde{\phi}} = 1$ but $N_{\tilde{\mu}_1} > 1$) is already enough to recover most of the lost information (see also Gagrani & Samushia 2017). However, it is necessary to also consider the variation of the bispectrum with respect to the azimuthal angle in order to further shrink the parameter constraints by 7 (for B) and 1.5 (for P and B combined) per cent. Note that our reference case represents a good

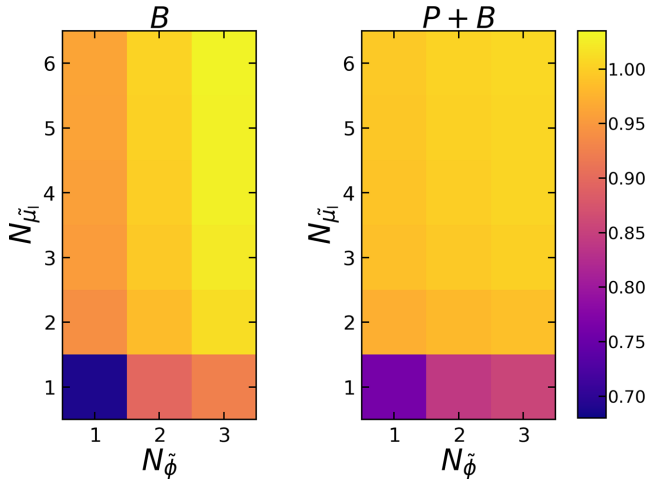

Figure 12. As in Fig. 10 but as a function of the number of bins used to describe the orientation of the triangular configuration of wavevectors with respect to the line of sight. Here, $N_{\tilde{\phi}}$ and $N_{\tilde{\mu}_1}$ denote the number of bins in the azimuthal angle $\tilde{\phi}$ and in the cosine of the polar angle $\tilde{\theta}$ (measured with respect to the longest wavevector), respectively. Shown is the quantity $\mathrm{FoM}^{1/n}$ evaluated for a generic $(N_{\tilde{\phi}}, N_{\tilde{\mu}_1})$ pair divided by the value it assumes for our reference case $N_{\tilde{\phi}} = 2$ and $N_{\tilde{\mu}_1} = 4$.

compromise between minimizing the number of bins and keeping most of the information contained in the data.

5.4 Shot-noise subtraction

In line with previous theoretical work (e.g. Sefusatti et al. 2006; Song et al. 2015; Gualdi et al. 2018b), the results presented in Section 4 quantify the cosmological dependence of the actual galaxy-clustering signal and thus assume that we can perfectly subtract the systematic shot-noise contributions to the power spectrum and the bispectrum. In a real survey, however, the mean galaxy density and the shot-noise corrections can only be estimated with some uncertainty (e.g. by using the selection function and the mask, Feldman et al. 1994; Scoccimarro 2000, 2015). Moreover, it is reasonable to expect that shot noise is not exactly Poissonian as evidenced by the analysis of mock catalogues based on N-body simulations (e.g. Mo & White 1996; Hamaus et al. 2010; Baldauf et al. 2013). Therefore, various approaches have been taken in the literature to generalize equations (25) and (26). For instance, in their analysis of the BOSS survey, Gil-Marín et al. (2014) rescale the shot-noise terms $P'_{\rm shot}$ and $B_{\rm shot}$ by the same constant factor that is then fit to the data. Similarly, Schmittfull, Baldauf & Seljak (2015) use two scale-independent factors to correct $P'_{\rm shot}$ and $B_{\rm shot}$ in order to fit the bispectrum of dark-matter haloes extracted from N-body simulations. This phenomenological approach can be motivated by writing a more general bias expansion that includes stochastic contributions (e.g. Dekel & Lahav 1999; Matsubara 1999; Angulo et al. 2015; Senatore 2015; Desjacques et al. 2018, and references therein). In this case, the term $\epsilon(\boldsymbol{x}) + \epsilon_1(\boldsymbol{x})\delta(\boldsymbol{x})$ should be added to the right-hand side of equation (17). Here, ϵ denotes the leading stochastic contribution to the bias relation, while ϵ_1 is the random part of the linear bias. By definition, both these fields have zero mean. Within these assumptions, it is straightforward to show that the power spectrum and the bispectrum of ϵ replace $P_{\rm shot}$ and $B_{\rm shot}$ in equations (25) and (26), respectively. On the other hand, the cross-spectrum between ϵ and ϵ_1 takes the place of $P'_{\rm shot}$ in equation (26). A popular strategy is to assume that, on large scales, these terms are approximately constant and somewhat close to the predictions of Poisson sampling. In this section, we explore the consequences of considering $P_{\rm shot}$, $P'_{\rm shot}$, and $B_{\rm shot}$ as three additional free parameters (using the fiducial values $n_{\rm g}^{-1}$, $n_{\rm g}^{-1}$, and $n_{\rm g}^{-2}$, respectively). The same approach has been adopted by Karagiannis et al. (2018) to study the constraining power of the galaxy bispectrum on primordial non-Gaussianity.

For the power spectrum, we find that fitting the amplitude of the additional white noise term, $P_{\rm shot}$, worsens the constraints on all cosmological parameters by between 21 and 32 per cent (the worst case being for $n_{\rm s}$) while basically leaves the errors on b_1 and $\sigma_{\rm p}$ unchanged.

A quick look at equation (26) shows that the situation is more complex for the bispectrum as the shot-noise contribution also contains a scale-dependent part that is proportional to the sum of three power spectra. For this reason, if we repeat the forecast presented in Section 4 by taking into account shot noise and assuming that (i) equation (26) exactly applies and (ii) we perfectly know $\bar{n}$, then most of the constraints on the fit parameters improve. The largest upgrades take place for $\Omega_{\rm cdm}$ (66 per cent), $n_{\rm s}$ (47 per cent), and A (44 per cent) while the smallest one applies to $\sigma_{\rm p}$ (30 per cent). Only the marginalized constraints in the non-linear bias parameters get slightly worse (by 7 per cent for b_2 and by 3.5 per cent for b_{s^2}).

We can now relax assumptions (i) and (ii) above by replacing $n_{\rm g}^{-1}$ and $n_{\rm g}^{-2}$ in equation (26) with two independent free parameters, $P'_{\rm shot}$ and $B_{\rm shot}$, that are then fit to the data including shot noise. After marginalizing the posteriors over $P'_{\rm shot}$ and $B_{\rm shot}$, we find that the constraints on b_{s^2} and $\sigma_{\rm p}$ worsen by nearly 50 and 30 per cent, respectively, compared with our reference case while those on the cosmological parameters improve nearly as much as in the example discussed in the previous paragraph.

Similar outcomes are found when we combine the power spectrum and the bispectrum: the constraint on $\Omega_{\rm cdm}$ improves by 55 per cent with respect to the corresponding reference case in Table 3, those on $n_{\rm s}$ and A by nearly 30 per cent, while the error on b_2 increases by a factor of 3. This happens because b_2 is degenerate with $B_{\rm shot}$. Using the *Planck* prior mitigates the differences. In this case, the uncertainties for all fit parameters deteriorate by less than 30–40 per cent with respect to the corresponding reference case.

The tests presented above have been performed at $z = 1$ where the systematic shot-noise contribution is ∼10 per cent of the actual clustering signal for both P and B. Of course, the impact of shot noise becomes more marked at higher redshifts were the number density of galaxies drops significantly. At $z \sim 2$, for instance, shot noise is comparable with the clustering signal.

Based on these results, we conclude that the treatment of shot noise in pure clustering studies (i.e. without external priors) has an impact on the resulting cosmological constraints and can alter them significantly. The tests performed here also suggests that our main analysis might be conservative for parameters like $\Omega_{\rm cdm}$, $n_{\rm s}$, and A.

5.5 Treatment of galaxy bias

In our main analysis, we have used three bias parameters per redshift bin (for a total of 42) and fit them independently to the data. This is the safest approach, as it does not rely on any other assumption than the bias expansion given in equation (17). However, it is reasonable to expect that the bias parameters change smoothly with redshift. In this case, it makes sense to approximate each of them with a simple fitting function that captures their variation. We consider here a quadratic function of redshift for each bias coefficient. This reduces the number of nuisance parameters with respect to our standard treatment from 42 to 9. Our results show that implementing this

simplified procedure does not give any practical advantage as the errors on the cosmological parameters basically remain unchanged with respect to our standard treatment.

6 SUMMARY AND CONCLUSIONS

Galaxy clustering is a powerful cosmological probe. Two-point statistics in configuration and Fourier space are routinely used to constrain models for our Universe. The question addressed in this paper is whether the galaxy bispectrum in redshift space contains additional information about the cosmological parameters.

The literature about the galaxy bispectrum mostly focuses either on the real-space statistic or on its redshift-space monopole. For this reason, in Section 3.2, we first illustrate the phenomenology of RSD for the bispectrum and explore different parametrizations for the spatial orientation of the triangles of wavevectors with respect to the line of sight. We then generalize the expressions found in the literature for the covariance matrix of bispectrum estimates and, in particular, for their cross-covariance with measurements of the power spectrum – see equation (42).

We use the Fisher information matrix to forecast constraints on a large number of cosmological and nuisance parameters from future measurements of the galaxy bispectrum and the power spectrum in redshift space. We consider flat FLRW models dominated by dark energy and CDM with Gaussian primordial perturbations. As an example of the forthcoming generation of experiments, we adopt the specifications of a *Euclid*-like galaxy redshift survey (Table 1). In our principal analysis, we only consider wavenumbers with $k \leq k_{\rm max} = 0.15\,h$ Mpc^{-1} that define mildly non-linear scales on which fluctuations in the galaxy density can be treated perturbatively. Within this range, it should thus be possible to build robust models for the galaxy power spectrum and bispectrum. The main conclusions of our work are as follows:

(i) The galaxy bispectrum and the power spectrum in redshift space set constraints of similar strength on the cosmological parameters (Table 3). Therefore, the bispectrum can be used as a consistency check for power-spectrum studies.

(ii) Posterior correlations between the model parameters derived from the bispectrum and the power spectrum are, in most cases, very similar (Figs 5–7). For this reason, combining the two probes only moderately improves the cosmological constraints with respect to considering them individually.

(iii) For instance, considering both statistics together partially breaks the degeneracies between the linear bias coefficients and the galaxy-clustering amplitudes in all redshift bins. In consequence, the FoM for the dark-energy parameters w_0 and w_a improves by a factor of 2.6 with respect to only using the power spectrum.

(iv) This advantage, however, vanishes once priors based on the results of the *Planck* mission and of current clustering studies are included in the analysis. In this case, combining the power spectrum with the bispectrum does not give any appreciable benefit other than precisely determining the parameters that describe galaxy bias.

(v) For wavenumbers $k < 0.15\,h$ Mpc^{-1}, the cross-covariance between the power spectrum and the bispectrum has a small influence on parameter estimation (Table 3) and may be safely neglected to first approximation.

(vi) Taking broad bins for the legs of the triangles of wavevectors leads to information loss for the bispectrum (Fig. 10). For instance, using $\Delta k = 5k_{\rm f}$ gives cosmological constraints that are suboptimal by 20 per cent.

(vii) Since the number of bins in the triangular configurations for the bispectrum grows more rapidly with the maximum wavenumber than the number of bands in the power spectrum, the relative importance of the two probes strongly depends on the value of $k_{\rm max}$ that is considered (Fig. 11). We find that, for $k_{\rm max} = 0.15\,h$ Mpc^{-1}, the power spectrum provides slightly tighter constraints than the bispectrum on most parameters. However, our results also suggest that the bispectrum becomes the leading probe if the analysis is extended beyond $k_{\rm max} \simeq 0.43\,h$ Mpc^{-1} (assuming that an accurate theoretical model is available at such wavenumbers).

(viii) RSD contain precious information about the cosmological parameters. Just considering the monopole moment of the bispectrum leads to a non-negligible loss of information. Individual error bars for the fit parameters typically grow by 50 per cent (Fig. 12). Taking into account the lowest-order non-vanishing multipoles with $m = 0$ recovers most of the lost information. Considering also variations of the bispectrum with the azimuthal angle further reduces the error bars by a few up to 10 per cent.

(ix) The way shot noise is handled in the clustering analysis influences the cosmological results (especially for $\Omega_{\rm cdm}$, $n_{\rm s}$, and A) as well as the non-linear bias parameter b_2. However, this dependence is significantly reduced by also considering CMB-based priors.

(x) Using a smooth function of redshift to describe the evolution of the bias coefficients does not lead to any practical advantage with respect to fitting individual parameters for every redshift bin.

ACKNOWLEDGEMENTS

We thank Emiliano Sefusatti for useful discussions and the anonymous reviewer for suggestions that helped improving the presentation of our results. We acknowledge financial support by the Deutsche Forschungsgemeinschaft through the Transregio 33 'The Dark Universe'. VY was also partly supported through a research contract from the International Max Planck Research School (IMPRS) for Astronomy and Astrophysics at the Universities of Bonn and Cologne and partially supported by the Bonn-Cologne Graduate School for Physics and Astronomy.

REFERENCES

Albrecht A. et al., 2006, preprint (arXiv:astro-ph/0609591)
Amendola L. et al., 2018, Living Rev. Relativ., 21, 2
Angulo R., Fasiello M., Senatore L., Vlah Z., 2015, J. Cosmol. Astropart. Phys., 9, 029
Angulo R. E., Baugh C. M., Frenk C. S., Lacey C. G., 2014, MNRAS, 442, 3256
Assassi V., Baumann D., Green D., Zaldarriaga M., 2014, J. Cosmol. Astropart. Phys., 8, 056
Baldauf T., Seljak U., Desjacques V., McDonald P., 2012, Phys. Rev. D, 86, 083540
Baldauf T., Seljak U., Smith R. E., Hamaus N., Desjacques V., 2013, Phys. Rev. D, 88, 083507
Baldauf T., Mercolli L., Mirbabayi M., Pajer E., 2015, J. Cosmol. Astropart. Phys., 5, 007
Baldauf T., Mirbabayi M., Simonović M., Zaldarriaga M., 2016, preprint (arXiv:1602.00674)
Ballinger W. E., Peacock J. A., Heavens A. F., 1996, MNRAS, 282, 877
Baugh C. M., Efstathiou G., 1993, MNRAS, 265, 145
Baumann D., Nicolis A., Senatore L., Zaldarriaga M., 2012, J. Cosmol. Astropart. Phys., 7, 051
Bel J., Hoffmann K., Gaztañaga E., 2015, MNRAS, 453, 259
Bernardeau F., Colombi S., Gaztañaga E., Scoccimarro R., 2002, Phys. Rep., 367, 1

Bertolini D., Schutz K., Solon M. P., Zurek K. M., 2016, J. Cosmol. Astropart. Phys., 6, 052
Beutler F. et al., 2014, MNRAS, 443, 1065
Bhattacharya S., Heitmann K., White M., Lukić Z., Wagner C., Habib S., 2011, ApJ, 732, 122
Bianchi D., Gil-Marín H., Ruggeri R., Percival W. J., 2015, MNRAS, 453, L11
Borzyszkowski M., Bertacca D., Porciani C., 2017, MNRAS, 471, 3899
Byun J., Eggemeier A., Regan D., Seery D., Smith R. E., 2017, MNRAS, 471, 1581
Carrasco J. J. M., Hertzberg M. P., Senatore L., 2012, J. High Energy Phys., 9, 82
Carron J., 2012, Phys. Rev. Lett., 108, 071301
Carron J., Neyrinck M. C., 2012, ApJ, 750, 28
Carron J., Szapudi I., 2014, MNRAS, 439, L11
Catelan P., Lucchin F., Matarrese S., Porciani C., 1998, MNRAS, 297, 692
Catelan P., Porciani C., Kamionkowski M., 2000, MNRAS, 318, L39
Chan K. C., Blot L., 2017, Phys. Rev. D, 96, 023528
Chan K. C., Scoccimarro R., Sheth R. K., 2012, Phys. Rev. D, 85, 083509
Chevallier M., Polarski D., 2001, Int. J. Mod. Phys. D, 10, 213
Cole S. et al., 2005, MNRAS, 362, 505
Crocce M., Scoccimarro R., Bernardeau F., 2012, MNRAS, 427, 2537
Croton D. J. et al., 2004, MNRAS, 352, 1232
Dekel A., Lahav O., 1999, ApJ, 520, 24
DESI Collaboration et al., 2016a, preprint (arXiv:1611.00036)
DESI Collaboration et al., 2016b, preprint (arXiv:1611.00037)
Desjacques V., Jeong D., Schmidt F., 2018, Phys. Rep., 733, 1
Eisenstein D. J. et al., 2005, ApJ, 633, 560
Feldman H. A., Kaiser N., Peacock J. A., 1994, ApJ, 426, 23
Fisher K. B., Scharf C. A., Lahav O., 1994, MNRAS, 266, 219
Fonseca de la Bella L., Regan D., Seery D., Hotchkiss S., 2017, J. Cosmol. Astropart. Phys., 11, 039
Frieman J. A., Gaztañaga E., 1999, ApJ, 521, L83
Fry J. N., 1994, Phys. Rev. Lett., 73, 215
Fry J. N., Gaztanaga E., 1993, ApJ, 413, 447
Fry J. N., Melott A. L., Shandarin S. F., 1993, ApJ, 412, 504
Gagrani P., Samushia L., 2017, MNRAS, 467, 928
Gaztañaga E., Norberg P., Baugh C. M., Croton D. J., 2005, MNRAS, 364, 620
Gaztañaga E., Cabré A., Castander F., Crocce M., Fosalba P., 2009, MNRAS, 399, 801
Geach J. E., Sobral D., Hickox R. C., Wake D. A., Smail I., Best P. N., Baugh C. M., Stott J. P., 2012, MNRAS, 426, 679
Gil-Marín H., Wagner C., Noreña J., Verde L., Percival W., 2014, J. Cosmol. Astropart. Phys., 12, 029
Gil-Marín H., Noreña J., Verde L., Percival W. J., Wagner C., Manera M., Schneider D. P., 2015, MNRAS, 451, 539
Gil-Marín H., Percival W. J., Verde L., Brownstein J. R., Chuang C.-H., Kitaura F.-S., Rodríguez-Torres S. A., Olmstead M. D., 2017, MNRAS, 465, 1757
Gonzalez-Perez V. et al., 2018, MNRAS, 474, 4024
Gualdi D., Gil-Marín H., Schuhmann R. L., Manera M., Joachimi B., Lahav O., 2018a, preprint (arXiv:1806.02853)
Gualdi D., Manera M., Joachimi B., Lahav O., 2018b, MNRAS, 476, 4045
Hamaus N., Seljak U., Desjacques V., Smith R. E., Baldauf T., 2010, Phys. Rev. D, 82, 043515
Hamilton A. J. S., 1998, in Hamilton D., ed., Astrophysics and Space Science Library Vol. 231, The Evolving Universe. Kluwer Academic Publishers, Dordrecht, p. 185
Hashimoto I., Rasera Y., Taruya A., 2017, Phys. Rev. D, 96, 043526
Heavens A. F., Taylor A. N., 1995, MNRAS, 275, 483
Hoffmann K., Bel J., Gaztañaga E., 2017, MNRAS, 465, 2225
Howlett C., Lewis A., Hall A., Challinor A., 2012, JCAP, 1204, 027
Jackson J. C., 1972, MNRAS, 156, 1P
Jing Y. P., Börner G., 1998, ApJ, 503, 37
Jing Y. P., Börner G., 2004, ApJ, 607, 140
Kaiser N., 1987, MNRAS, 227, 1
Karagiannis D., Lazanu A., Liguori M., Raccanelli A., Bartolo N., Verde L., 2018, MNRAS, 478, 1341
Kayo I., Takada M., Jain B., 2013, MNRAS, 429, 344
Kazin E. A., Sánchez A. G., Blanton M. R., 2012, MNRAS, 419, 3223
Kulkarni G. V., Nichol R. C., Sheth R. K., Seo H.-J., Eisenstein D. J., Gray A., 2007, MNRAS, 378, 1196
Kuruvilla J., Porciani C., 2018, MNRAS, 479, 2256
Laureijs R. et al., 2011, preprint (arXiv:1110.3193)
Lazanu A., Giannantonio T., Schmittfull M., Shellard E. P. S., 2016, Phys. Rev. D, 93, 083517
Lazeyras T., Wagner C., Baldauf T., Schmidt F., 2016, J. Cosmol. Astropart. Phys., 2, 018
Lewis A., Challinor A., Lasenby A., 2000, ApJ, 538, 473
Lin H., Kirshner R. P., Shectman S. A., Landy S. D., Oemler A., Tucker D. L., Schechter P. L., 1996, ApJ, 471, 617
Linder E. V., 2003, Phys. Rev. Lett., 90, 091301
Lucy L. B., 1974, AJ, 79, 745
Maartens R., Abdalla F. B., Jarvis M., Santos M. G., 2015, Advancing Astrophysics with the Square Kilometre Array (AASKA14), p. 16, http://adsabs.harvard.edu/abs/2015aska.confE..16M
Marín F., 2011, ApJ, 737, 97
Matarrese S., Verde L., Heavens A. F., 1997, MNRAS, 290, 651
Matsubara T., 1999, ApJ, 525, 543
Matsubara T., 2008, Phys. Rev. D, 77, 063530
McDonald P., Roy A., 2009, J. Cosmol. Astropart. Phys., 8, 020
Mehrem R., 2009, preprint (arXiv:0909.0494)
Meiksin A., White M., 1999, MNRAS, 308, 1179
Mohammed I., Seljak U., Vlah Z., 2017, MNRAS, 466, 780
Moradinezhad Dizgah A., Lee H., Muñoz J. B., Dvorkin C., 2018, J. Cosmol. Astropart. Phys., 5, 013
Mortonson M. J., Huterer D., Hu W., 2010, Phys. Rev. D, 82, 063004
Mo H. J., White S. D. M., 1996, MNRAS, 282, 347
Neyrinck M. C., Szapudi I., 2007, MNRAS, 375, L51
Nichol R. C. et al., 2006, MNRAS, 368, 1507
Orsi A., Baugh C. M., Lacey C. G., Cimatti A., Wang Y., Zamorani G., 2010, MNRAS, 405, 1006
Pápai P., Szapudi I., 2008, MNRAS, 389, 292
Peacock J. A., 1992, in Martinez V. J., Portilla M., Saez D., eds, Lecture Notes in Physics, Vol. 408, New Insights into the Universe. Springer Verlag, Berlin, p. 1
Peacock J. A., Dodds S. J., 1994, MNRAS, 267, 1020
Planck Collaboration et al., 2016, A&A, 594, A13
Pozzetti L. et al., 2016, A&A, 590, A3
Rimes C. D., Hamilton A. J. S., 2005, MNRAS, 360, L82
Sahni V., Starobinsky A., 2006, Int. J. Mod. Phys. D, 15, 2105
Saito S., Baldauf T., Vlah Z., Seljak U., Okumura T., McDonald P., 2014, Phys. Rev. D, 90, 123522
Sargent W. L. W., Turner E. L., 1977, ApJ, 212, L3
Scherrer R. J., 2015, Phys. Rev. D, 92, 043001
Schmittfull M., Baldauf T., Seljak U., 2015, Phys. Rev. D, 91, 043530
Scoccimarro R., 2000, ApJ, 544, 597
Scoccimarro R., 2004, Phys. Rev. D, 70, 083007
Scoccimarro R., 2015, Phys. Rev. D, 92, 083532
Scoccimarro R., Colombi S., Fry J. N., Frieman J. A., Hivon E., Melott A., 1998, ApJ, 496, 586
Scoccimarro R., Couchman H. M. P., Frieman J. A., 1999a, ApJ, 517, 531
Scoccimarro R., Zaldarriaga M., Hui L., 1999b, ApJ, 527, 1
Scoccimarro R., Feldman H. A., Fry J. N., Frieman J. A., 2001, ApJ, 546, 652
Scoccimarro R., Sefusatti E., Zaldarriaga M., 2004, Phys. Rev. D, 69, 103513
Sefusatti E., Komatsu E., 2007, Phys. Rev. D, 76, 083004
Sefusatti E., Crocce M., Pueblas S., Scoccimarro R., 2006, Phys. Rev. D, 74, 023522
Senatore L., 2015, J. Cosmol. Astropart. Phys., 11, 007
Sheth R. K., Mo H. J., Tormen G., 2001, MNRAS, 323, 1
Slepian Z. et al., 2017, MNRAS, 468, 1070
Song Y.-S., Taruya A., Oka A., 2015, J. Cosmol. Astropart. Phys., 8, 007

Takahashi R. et al., 2009, ApJ, 700, 479
Taruya A., Saito S., Nishimichi T., 2011, Phys. Rev. D, 83, 103527
Taylor A. N., Hamilton A. J. S., 1996, MNRAS, 282, 767
Tegmark M., Taylor A. N., Heavens A. F., 1997, ApJ, 480, 22
Tellarini M., Ross A. J., Tasinato G., Wands D., 2016, J. Cosmol. Astropart. Phys., 6, 014
Verde L. et al., 2002, MNRAS, 335, 432
Vogeley M. S., Szalay A. S., 1996, ApJ, 465, 34
Wang Y., 2008, Phys. Rev. D, 77, 123525
Yamauchi D., Yokoyama S., Takahashi K., 2017a, Phys. Rev. D, 95, 063530
Yamauchi D., Yokoyama S., Tashiro H., 2017b, Phys. Rev. D, 96, 123516

APPENDIX A: COORDINATE SYSTEMS

We introduce here two different coordinate systems in order to parametrize the relative orientation between a triangle of wavevectors and the line of sight.

A1 Using the triangle's normal as the polar axis

Let us consider a triangle of sides $\boldsymbol{k}_1, \boldsymbol{k}_2$, and $\boldsymbol{k}_3$ such that $\boldsymbol{k}_1 + \boldsymbol{k}_2 + \boldsymbol{k}_3 = 0$. The triangle lies on a plane whose normal vector is parallel to $\boldsymbol{n} = \boldsymbol{k}_1 \times \boldsymbol{k}_2$. The orientation of the unit vector $\hat{\boldsymbol{n}} = \boldsymbol{n}/||\boldsymbol{n}||$ with respect to the line-of-sight direction $\hat{\boldsymbol{s}}$ can be described in terms of a single rotation around the axis $\boldsymbol{w} = \hat{\boldsymbol{n}} \times \hat{\boldsymbol{s}}$ (see Fig. A1). We want to build a right-handed orthonormal basis starting from $\hat{\boldsymbol{s}}$ and $\hat{\boldsymbol{w}}$. For the third element of the basis, we pick a unit vector $\hat{\boldsymbol{u}}$ parallel to $\hat{\boldsymbol{s}} \times \hat{\boldsymbol{w}} = \hat{\boldsymbol{n}} - (\hat{\boldsymbol{n}} \cdot \hat{\boldsymbol{s}})\,\hat{\boldsymbol{s}}$, i.e. $\hat{\boldsymbol{u}} = (\hat{\boldsymbol{n}} - (\hat{\boldsymbol{n}} \cdot \hat{\boldsymbol{s}})\,\hat{\boldsymbol{s}})/\sqrt{1 - (\hat{\boldsymbol{n}} \cdot \hat{\boldsymbol{s}})^2}$. In the base $\hat{\boldsymbol{w}}, \hat{\boldsymbol{u}}, \hat{\boldsymbol{s}}$, the rotation from $\hat{\boldsymbol{n}}$ to $\hat{\boldsymbol{s}}$ is described by the matrix,

$$\mathbf{R} = \begin{pmatrix} 1 & 0 & 0 \\ 0 & \hat{\boldsymbol{n}} \cdot \hat{\boldsymbol{s}} & -||\hat{\boldsymbol{n}} \times \hat{\boldsymbol{s}}|| \\ 0 & ||\hat{\boldsymbol{n}} \times \hat{\boldsymbol{s}}|| & \hat{\boldsymbol{n}} \cdot \hat{\boldsymbol{s}} \end{pmatrix} . \tag{A1}$$

In fact, $\hat{\boldsymbol{n}}$ is a column vector with coordinates

$$(\hat{\boldsymbol{n}} \cdot \hat{\boldsymbol{w}}, \hat{\boldsymbol{n}} \cdot \hat{\boldsymbol{u}}, \hat{\boldsymbol{n}} \cdot \hat{\boldsymbol{s}}) = (0, \sqrt{1 - (\hat{\boldsymbol{n}} \cdot \hat{\boldsymbol{s}})^2}, \hat{\boldsymbol{n}} \cdot \hat{\boldsymbol{s}}) \tag{A2}$$

and applying the rotation to it one gets (0,0,1). This is a rotation by an angle $0 \leq \omega < \pi$ such that $\cos\omega = \hat{\boldsymbol{n}} \cdot \hat{\boldsymbol{s}}$ and $\sin\omega = ||\hat{\boldsymbol{n}} \times \hat{\boldsymbol{s}}|| = ||\boldsymbol{w}||$ (note than $\sin\omega \geq 0$). This completely describes the relative orientation of the plane of the triangle with respect to the line of sight.

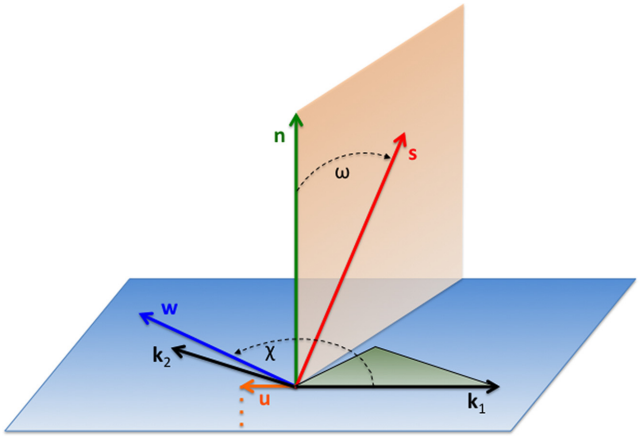

Figure A1. Schematic showing the definition of the angles (ω, χ).

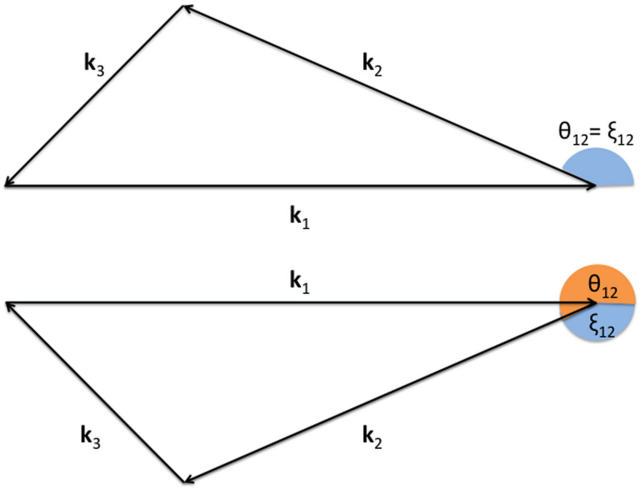

Figure A2. Definition of the angles θ_{12} and ξ_{12} for two triangles with the same shape but opposite handedness.

Now, we only need to describe the orientation of the triangle on its plane. Note that, being perpendicular to $\hat{\boldsymbol{n}}$, the basis element $\hat{\boldsymbol{w}}$ lies on the plane of the triangle. It is thus convenient to measure the orientation of the triangle in its plane by looking at the orientation of, say, $\boldsymbol{k}_1$ with respect to $\hat{\boldsymbol{w}}$. In order to quantify this, we introduce the angle χ $(0 \leq \chi < 2\pi)$ such that $\hat{\boldsymbol{k}}_1 \cdot \hat{\boldsymbol{w}} = \cos\chi$ and $(\hat{\boldsymbol{k}}_1 \times \hat{\boldsymbol{w}}) \cdot \hat{\boldsymbol{n}} = \sin\chi$. It is worth stressing that $\hat{\boldsymbol{k}}_1 \times \hat{\boldsymbol{w}} = \hat{\boldsymbol{k}}_1 \times (\hat{\boldsymbol{n}} \times \hat{\boldsymbol{s}})/||\boldsymbol{w}|| = (\hat{\boldsymbol{k}}_1 \cdot \hat{\boldsymbol{s}})\,\hat{\boldsymbol{n}}/||\boldsymbol{w}||$ and $\sin\chi = (\hat{\boldsymbol{k}}_1 \cdot \hat{\boldsymbol{s}})/||\boldsymbol{w}|| = \mu_1/\sin\omega$. The angle χ denotes the rotation angle around $\hat{\boldsymbol{n}}$ from $\hat{\boldsymbol{k}}_1$ to $\hat{\boldsymbol{w}}$.

Let us now reverse the problem and determine the line-of-sight components of $\boldsymbol{k}_1, \boldsymbol{k}_2, \boldsymbol{k}_3$ for given ω and χ. The shape and the handedness of the triangle matter. A common choice is to parametrize the relative orientation of $\boldsymbol{k}_1$ and $\boldsymbol{k}_2$ in terms of the angle θ_{12} such that $\hat{\boldsymbol{k}}_2 \cdot \hat{\boldsymbol{k}}_1 = \cos\theta_{12}$ and $||\boldsymbol{n}|| = ||\boldsymbol{k}_1 \times \boldsymbol{k}_2|| = |\sin\theta_{12}|$. In principle, $0 \leq \theta_{12} < 2\pi$ and, for a fixed shape, triangles with θ_{12} and $2\pi - \theta_{12}$ have opposite handedness (see Fig. A2). However, $\hat{\boldsymbol{n}}$, $\hat{\boldsymbol{w}}$, and $\hat{\boldsymbol{u}}$ flip sign when the handedness is switched. It is thus much more convenient to express the shape of the triangle in terms of a rotation angle around $\hat{\boldsymbol{n}}$ and always use an angle ξ_{12} such that $0 \leq \xi_{12} < \pi$ and $\sin\xi_{12} \geq 0$. In words, $\xi_{12} = \arccos(\hat{\boldsymbol{k}}_1 \cdot \hat{\boldsymbol{k}}_2)$ is the (shortest) rotation angle around $\hat{\boldsymbol{n}}$ from $\hat{\boldsymbol{k}}_1$ to $\hat{\boldsymbol{k}}_2$. Triangles with the same shape but opposite handedness have identical ξ_{12}.

We recall that, using the vector basis we have introduced above, $\hat{\boldsymbol{n}} = (0, \sin\omega, \cos\omega)$ and $\hat{\boldsymbol{s}} = (0, 0, 1)$, so that $\boldsymbol{w} = (\sin\omega, 0, 0)$ and $\boldsymbol{u} = (0, \sin\omega, 0)$. From the definitions $\hat{\boldsymbol{k}}_1 \cdot \hat{\boldsymbol{w}} = \cos\chi$ and $(\hat{\boldsymbol{k}}_1 \times \hat{\boldsymbol{w}}) \cdot \hat{\boldsymbol{n}} = \sin\chi$, it follows that

$$\boldsymbol{k}_1 = k_1\,(\cos\chi, -\cos\omega\sin\chi, \sin\omega\sin\chi). \tag{A3}$$

Since the vector $\hat{\boldsymbol{k}}_2$ corresponds to a rotation of $\hat{\boldsymbol{k}}_1$ by an angle ξ_{12} around $\hat{\boldsymbol{n}}$, while $\hat{\boldsymbol{w}}$ is rotated from $\hat{\boldsymbol{k}}_1$ by an angle χ around $\hat{\boldsymbol{n}}$, it follows that

$$\boldsymbol{k}_2 = k_2\,(\cos(\chi - \xi_{12}), -\cos\omega\sin(\chi - \xi_{12}), \sin\omega\sin(\chi - \xi_{12}))\ . \tag{A4}$$

This univocally fixes the RSD:

$$\mu_1 = \sin\omega\sin\chi\,, \tag{A5}$$

$$\mu_2 = \sin\omega\sin(\chi - \xi_{12}). \tag{A6}$$

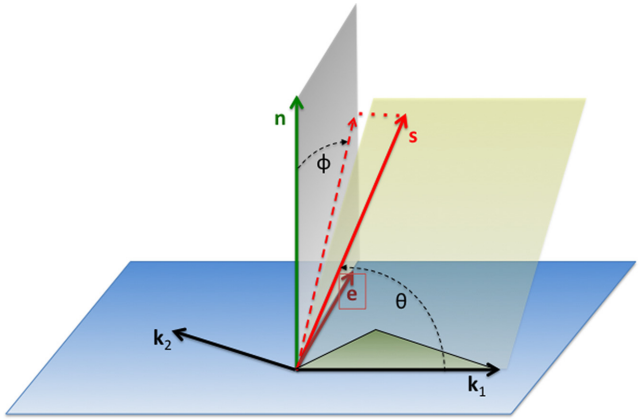

Figure A3. Schematic showing the definition of the angles (θ, ϕ).

A2 Using k_1 as the polar axis

Scoccimarro et al. (1999a) use a different parametrization in terms of the polar angle $0 \leq \theta < \pi$ and the azimuthal angle $0 \leq \phi < 2\pi$ that define the orientation of $\hat{\boldsymbol{s}}$ with respect to $\hat{\boldsymbol{k}}_1$ (see Fig. A3). In order to link this approach to our previous discussion, let us build a right-handed orthonormal basis by complementing $\hat{\boldsymbol{n}}$ and $\hat{\boldsymbol{k}}_1$ with another unit vector $\hat{\boldsymbol{e}}$ lying in the plane of the triangle – i.e. $\hat{\boldsymbol{e}}$ is the unit vector of $\boldsymbol{e} = \boldsymbol{n} \times \boldsymbol{k}_1 = k_1^2 \boldsymbol{k}_2 - (\boldsymbol{k}_1 \cdot \boldsymbol{k}_2)\boldsymbol{k}_1$ or $\hat{\boldsymbol{e}} = [\hat{\boldsymbol{k}}_2 - (\hat{\boldsymbol{k}}_1 \cdot \hat{\boldsymbol{k}}_2)\hat{\boldsymbol{k}}_1]/\sqrt{1-(\hat{\boldsymbol{k}}_1 \cdot \hat{\boldsymbol{k}}_2)^2}$. In the basis $(\hat{\boldsymbol{k}}_1, \hat{\boldsymbol{e}}, \hat{\boldsymbol{n}})$, $\hat{\boldsymbol{k}}_2$ is a column vector of coordinates $(\cos\xi_{12}, \sin\xi_{12}, 0)$ – note once again that both $\hat{\boldsymbol{n}}$ and $\hat{\boldsymbol{e}}$ flip sign if the handedness of the triangle is changed and this is why we can use ξ_{12} instead of θ_{12}. For the azimuth ϕ, we use the angle between $\hat{\boldsymbol{n}}$ and the projection of $\hat{\boldsymbol{s}}$ on the plane defined by $\hat{\boldsymbol{n}}$ and $\hat{\boldsymbol{e}}$. This means that $\cos\phi = 0$ (i.e. $\phi = \pi/2$ or $3\pi/2$) whenever $\hat{\boldsymbol{s}}$ lies on the plane of triangle. Given all this, in the basis $(\hat{\boldsymbol{k}}_1, \hat{\boldsymbol{e}}, \hat{\boldsymbol{n}})$, $\hat{\boldsymbol{s}}$ is the column vector of coordinates $(\cos\theta, \sin\theta\ \sin\phi, \sin\theta\ \cos\phi)$ so that

$$\mu_1 = \cos\theta, \tag{A7}$$

$$\mu_2 = \cos\theta\cos\xi_{12} + \sin\theta\sin\phi\sin\xi_{12}. \tag{A8}$$

For generic vectors $\boldsymbol{k}_1$, $\boldsymbol{k}_2$, and $\hat{\boldsymbol{s}}$ defined in an arbitrary basis (e.g. a Fourier grid used to measure the bispectrum in a numerical simulation or for a galaxy catalogue), the angles θ and ϕ can be determined as follows. The polar angle is simply given by $\theta = \arccos(\hat{\boldsymbol{k}}_1 \cdot \hat{\boldsymbol{s}})$. For the azimuth, instead, it is convenient to introduce the vector $\boldsymbol{s}_\perp = \hat{\boldsymbol{s}} - (\hat{\boldsymbol{s}} \cdot \hat{\boldsymbol{k}}_1)\hat{\boldsymbol{k}}_1$ (which gives the component of $\hat{\boldsymbol{s}}$ perpendicular to $\boldsymbol{k}_1$) and calculate the real numbers $\cos\phi = \hat{\boldsymbol{s}}_\perp \cdot \hat{\boldsymbol{n}} = (\hat{\boldsymbol{s}} \cdot \hat{\boldsymbol{n}})/||\boldsymbol{s}_\perp|| = \sigma_n$ and $\sin\phi = \hat{\boldsymbol{s}}_\perp \cdot \hat{\boldsymbol{e}} = (\hat{\boldsymbol{s}} \cdot \hat{\boldsymbol{e}})/||\boldsymbol{s}_\perp|| = \sigma_e$. If $\sin\phi > 0$, then $\phi = \arccos(\sigma_n)$ while, if $\sin\phi < 0$, $\phi = 2\pi - \arccos(\sigma_n)$.

A3 Matching the different coordinate systems

Starting from the expressions for $\boldsymbol{k}_1$, $\boldsymbol{k}_2$, and $\boldsymbol{s}$ in the (θ, ϕ) coordinates and applying the definitions of the angles ω and χ, one obtains

$$\cos\omega = \sin\theta\cos\phi\ , \tag{A9}$$

$$\sin\omega = \sqrt{1-\sin^2\theta\cos^2\phi}\ , \tag{A10}$$

$$\cos\chi = \frac{-\sin\theta\sin\phi}{\sqrt{1-\sin^2\theta\cos^2\phi}}\ , \tag{A11}$$

$$\sin\chi = \frac{\cos\theta}{\sqrt{1-\sin^2\theta\cos^2\phi}}\ . \tag{A12}$$

Vice versa, starting from the expressions in terms of (ω, χ), one derives

$$\cos\theta = \sin\omega\sin\chi, \tag{A13}$$

$$\sin\theta = \sqrt{1-\sin^2\omega\sin^2\chi}, \tag{A14}$$

$$\cos\phi = \frac{\cos\omega}{\sqrt{1-\sin^2\omega\sin^2\chi}}, \tag{A15}$$

$$\sin\phi = \frac{-\sin\omega\cos\chi}{\sqrt{1-\sin^2\omega\sin^2\chi}}. \tag{A16}$$

A4 Symmetries

RSD are quadratic in the μ_i and do not change if μ_1, μ_2, and μ_3 change sign simultaneously. In terms of the (θ, ϕ) variables, this means that the galaxy bispectrum in redshift space is symmetric with respect to the transformation

$$\begin{cases} \theta \to \pi - \theta, \\ \phi \to 2\pi - \phi. \end{cases} \tag{A17}$$

In fact, by considering equations (A7) and (A8), one can easily prove that this transformation changes sign to μ_1, μ_2, and μ_3. This means that the (θ, ϕ) variables are somewhat redundant and not all the parameter space they cover is necessary to describe the RSD. It is thus appealing to seek for new angular coordinates that make the necessary region more compact and do not present duplications. In fact, this helps reduce the number of bins needed to represent all possible configurations. For instance, we can halve the size of parameter space by introducing a new set of coordinates $(\tilde{\theta}, \phi')$ such that $\tilde{\theta} = \min(\theta, \pi - \theta)$ and

$$\phi' = \begin{cases} \phi\ , & \text{if } \theta < \pi/2\ , \\ 2\pi - \phi\ , & \text{otherwise.} \end{cases} \tag{A18}$$

In this case, $0 \leq \tilde{\theta} < \pi/2$ (or $0 < \tilde{\mu} = \cos\tilde{\theta} \leq 1$) and $0 \leq \phi' < 2\pi$. However, RSD possess still another symmetry deriving from the fact that they only depend on $\sin\phi$ (and, equivalently, on $\sin\phi'$). Since, $\sin(\pi - x) = \sin x$, we can further halve the area of parameter space by introducing the variable $\pi/2 \leq \tilde{\phi} < 3\pi/2$ defined as follows:

$$\tilde{\phi} = \begin{cases} \pi - \phi'\ , & \text{if } 0 \leq \phi' < \pi/2, \\ \phi'\ , & \text{if } \pi/2 \leq \phi' < 3\pi/2, \\ 3\pi - \phi'\ , & \text{if } 3\pi/2 \leq \phi' < 2\pi. \end{cases} \tag{A19}$$

The angular variables $\tilde{\theta}$ and $\tilde{\phi}$ are optimal in the sense that they suffice to describe all possible configurations while minimizing the size of parameter space.

Similarly, we can derive optimal variables also starting from the coordinates (ω, χ). Equations (A5) and (A6) show that μ_1 and μ_2 change sign if $\chi \to \pi + \chi$, while ω is left unchanged. It follows that considering the variable $0 \leq \tilde{\chi} < \pi$ defined as

$$\tilde{\chi} = \begin{cases} \chi, & \text{if } \chi < \pi \\ \chi - \pi, & \text{otherwise} \end{cases} \tag{A20}$$

is sufficient to identify the configurations with opposite signs of μ_1 and μ_2. In fact, under the transformation $\theta \to \pi - \theta$ and $\phi \to 2\pi - \phi$, ω is unchanged while both $\cos\chi$ and $\sin\chi$ change sign that corresponds to the transformation $\chi \to \pi + \chi$. The second symmetry, in this case, derives from the fact that the RSD only depend on $\sin\omega$. Therefore, we can further reduce the extension of parameter space by introducing the variable $\tilde{\omega} = \min(\omega, \pi - \omega)$ so that $\cos\tilde{\omega} = |\cos\omega|$. The set $(\tilde{\omega}, \tilde{\chi})$ is optimal.

APPENDIX B: BIAS PARAMETERS

In Table B1, we report the forecast errors for the galaxy-bias parameters corresponding to our main analysis presented in Section 4.

Table B1. Expected marginalized 1σ errors for the galaxy bias parameters b_1, b_2, and b_{s^2} in the ΛCDM, wCDM and w_0w_aCDM models obtained considering a *Euclid*-like survey. The different rows display results obtained from the galaxy power spectrum (P, only for b_1), the bispectrum (B), and their combination ($P + B$) for 14 redshift bins centred at redshift z (different columns).

Probe	Parameter	0.7	0.8	0.9	1.0	1.1	1.2	1.3	1.4	1.5	1.6	1.7	1.8	1.9	2.0
							ΛCDM model								
P	b_1	0.014	0.014	0.015	0.016	0.017	0.017	0.018	0.019	0.020	0.021	0.022	0.023	0.024	0.026
B	b_1	0.046	0.048	0.051	0.053	0.056	0.060	0.066	0.072	0.085	0.097	0.120	0.157	0.189	0.253
$P + B$	b_1	0.012	0.012	0.013	0.013	0.014	0.014	0.015	0.015	0.016	0.017	0.018	0.019	0.020	0.022
B	b_2	0.062	0.064	0.070	0.073	0.080	0.089	0.105	0.125	0.164	0.203	0.272	0.384	0.488	0.684
$P + B$	b_2	0.014	0.015	0.016	0.016	0.017	0.019	0.023	0.027	0.035	0.043	0.057	0.079	0.099	0.137
B	b_{s^2}	0.143	0.144	0.156	0.159	0.175	0.194	0.230	0.270	0.355	0.432	0.572	0.795	0.992	1.365
$P + B$	b_{s^2}	0.070	0.071	0.077	0.079	0.086	0.096	0.113	0.132	0.173	0.210	0.277	0.384	0.479	0.658
							wCDM model								
P	b_1	0.024	0.027	0.029	0.032	0.034	0.037	0.039	0.042	0.044	0.047	0.050	0.052	0.055	0.058
B	b_1	0.071	0.077	0.084	0.091	0.099	0.108	0.117	0.127	0.142	0.155	0.176	0.209	0.239	0.296
$P + B$	b_1	0.016	0.017	0.019	0.020	0.022	0.023	0.025	0.027	0.028	0.030	0.032	0.034	0.036	0.038
B	b_2	0.074	0.077	0.084	0.088	0.097	0.107	0.123	0.142	0.180	0.218	0.285	0.394	0.497	0.691
$P + B$	b_2	0.015	0.015	0.016	0.016	0.018	0.019	0.023	0.027	0.035	0.043	0.057	0.080	0.100	0.138
B	b_{s^2}	0.146	0.147	0.158	0.160	0.175	0.194	0.230	0.270	0.355	0.433	0.573	0.795	0.993	1.366
$P + B$	b_{s^2}	0.073	0.075	0.081	0.084	0.092	0.102	0.119	0.138	0.178	0.215	0.282	0.388	0.483	0.661
							w_0w_aCDM model								
P	b_1	0.045	0.048	0.052	0.056	0.060	0.065	0.069	0.074	0.079	0.085	0.090	0.095	0.101	0.106
B	b_1	0.090	0.095	0.101	0.107	0.115	0.124	0.134	0.145	0.160	0.175	0.196	0.228	0.259	0.315
$P + B$	b_1	0.019	0.020	0.022	0.023	0.025	0.027	0.029	0.031	0.033	0.035	0.038	0.040	0.043	0.045
B	b_2	0.087	0.089	0.093	0.096	0.103	0.112	0.127	0.146	0.183	0.220	0.287	0.395	0.498	0.692
$P + B$	b_2	0.015	0.015	0.016	0.016	0.018	0.019	0.023	0.027	0.035	0.044	0.058	0.080	0.101	0.138
B	b_{s^2}	0.147	0.147	0.158	0.161	0.176	0.195	0.231	0.271	0.356	0.434	0.574	0.796	0.993	1.366
$P + B$	b_{s^2}	0.077	0.078	0.084	0.087	0.095	0.105	0.122	0.141	0.181	0.218	0.284	0.389	0.484	0.663

This paper has been typeset from a TEX/LATEX file prepared by the author.